LAWRENCE
LIVERMORE
NATIONAL
LABORATORY

UCRL-TR-230335

Electrochemical Studies of Passive Film Stability on Fe49.7Cr17.7Mn1.9Mo7.4W1.6B15.2C3.8Si2.4 Amorphous Metal in Seawater at 90oCElectrochemical Studies of Passive Film Stability on

Fe49.7Cr17.7Mn1.9Mo7.4W1.6B15.2C3.8Si2.4 Amorphous Metal in Seawater at 90C61616;C

J.C. Farmer, J. Haslam, S.D. Day, T. Lian, C.K. Saw, P.D. Hailey, J-S. Choi, R.B. Rebak, N. Yang, J.H. Payer, J.H. Perepezko, K. Hildal, E.J. Lavernia, L. Ajdelsztajn, D.J. Branagan, E.J. Buffa, L.F. Aprigliano

April 30, 2007

This work was performed under the auspices of the U.S. Department of Energy by University of California, Lawrence Livermore National Laboratory under Contract W-7405-Eng-48

Electrochemical Studies of Passive Film Stability on $Fe_{49.7}Cr_{17.7}Mn_{1.9}Mo_{7.4}W_{1.6}B_{15.2}C_{3.8}Si_{2.4}$ Amorphous Metal in Seawater at 90°C

J. C. Farmer, J. J. Haslam, S. D. Day, T. Lian, C. K. Saw, P. D. Hailey, J-S. Choi & R. B. Rebak
Lawrence Livermore National Laboratory, Livermore, California

N. Yang
Sandia National Laboratory, Livermore, California

J. H. Payer
Case Western Reserve University, Cleveland, Ohio

J. H. Perepezko & K. Hildal
University of Wisconsin, Madison, Wisconsin

E. J. Lavernia & L. Ajdelsztajn
University of California, Davis, California

D. J. Branagan & E. J. Buffa
The NanoSteel Company, Idaho Falls, Idaho

L. F. Aprigliano
Strategic Analysis, Arlington, Virginia

An iron-based amorphous metal, $Fe_{49.7}Cr_{17.7}Mn_{1.9}Mo_{7.4}W_{1.6}B_{15.2}C_{3.8}Si_{2.4}$ (SAM2X5), with very good corrosion resistance was developed. This material was prepared as a melt-spun ribbon, as well as gas atomized powder and a thermal-spray coating. During electrochemical testing in several environments, including seawater at 90°C, the passive film stability was found to be comparable to that of high-performance nickel-based alloys, and superior to that of stainless steels, based on electrochemical measurements of the passive film breakdown potential and general corrosion rates. This material also performed very well in standard salt fog tests. Chromium (Cr), molybdenum (Mo) and tungsten (W) provided corrosion resistance, and boron (B) enabled glass formation. The high boron content of this particular amorphous metal made it an effective neutron absorber, and suitable for criticality control applications. This material and its parent alloy maintained corrosion resistance up to the glass transition temperature, and remained in the amorphous state during exposure to relatively high neutron doses.

I. INTRODUCTION

The outstanding corrosion resistance that may be possible with amorphous metals was recognized several years ago.[1-4] Compositions of several iron-based amorphous metals were published, including several with very good corrosion resistance. Examples included: thermally sprayed coatings of Fe-10Cr-10-Mo-(C,B), bulk Fe-Cr-Mo-C-B, and Fe-Cr-Mo-C-B-P.[5-7] The corrosion resistance of an iron-based amorphous alloy with yttrium, $Fe_{48}Mo_{14}Cr_{15}Y_2C_{15}B_6$, was also established.[8-12] Yttrium was added to this alloy to lower the critical cooling rate. In addition to iron-based materials, several nickel-based amorphous metals were developed that exhibit exceptional corrosion performance in acids.[13] Very good thermal spray coatings of nickel-based crystalline coatings were deposited with thermal spray, but appear to have less corrosion resistance than nickel-based amorphous coatings.[14]

Several iron-based amorphous alloys have been developed with very good corrosion resistance. Most of these alloys are based upon a common parent alloy, and can be applied as thermal spray coatings.[15-16] One of the most promising formulations is $Fe_{49.7}Cr_{17.7}Mn_{1.9}Mo_{7.4}W_{1.6}B_{15.2}C_{3.8}Si_{2.4}$ (SAM2X5), which includes chromium (Cr), molybdenum (Mo), and tungsten (W) for enhanced corrosion resistance, and boron (B) to enable glass formation and neutron absorption. This alloy was recently discussed at a meeting of the Materials Research Society in regard to its beneficial application to the safe storage of spent nuclear fuel.[17-19] The target compositions of this alloy, other amorphous alloys in the same family, and crystalline alloys such as Type 316L stainless steel (UNS # S31603) and nickel-based Alloy C-22 (UNS # N06022) are given in Table I.

Conclusions regarding the exceptional passive film stability and corrosion resistance of this iron-based amorphous alloy compared to crystalline reference materials were based on measurements of passive film breakdown potential and corrosion rate, as well as observed performance during salt fog testing. Such measurements enabled the corrosion performance of various iron-based amorphous alloys, carbon steel, iron-based stainless steels and nickel-based alloys to be directly compared.

The resistance to localized corrosion is quantified through measurement of the open-circuit corrosion potential (E_{corr}), the breakdown or critical potential ($E_{critical}$), and the repassivation potential (E_{rp}). The greater the difference between the open-circuit corrosion potential and the critical potential (ΔE), the more resistant a material is to modes of localized corrosion such a pitting and crevice corrosion. Spontaneous breakdown of the passive film and localized corrosion require that the open-circuit corrosion potential exceed the critical potential:

$$E_{corr} \geq E_{critical} \quad (1)$$

General corrosion is assumed when E_{corr} is less than $E_{critical}$ ($E_{corr} < E_{critical}$), and localized corrosion is assumed when E_{corr} exceeds $E_{critical}$.[20] Measured values of the repassivation potential (E_{rp}) are sometimes used as conservative estimates of the critical potential ($E_{critical}$).

In the published scientific literature, different bases exist for determining the critical potential from electrochemical measurements.[21-22] The breakdown or critical potential has been defined as the potential where the passive current density increases to a level between 1 to 10 $\mu A/cm^2$ (10^{-6} to 10^{-5} A/cm^2) while increasing potential in the positive (anodic) direction during cyclic polarization or potential-step testing. The repassivation potential has been defined as the potential where the current density drops to a level indicative of passivity, which has been

assumed to be between 0.1 to 1.0 μA/cm^2 (10^{-6} to 10^{-7} A/cm^2), while decreasing potential from the maximum level reached during cyclic polarization or potential-step testing. Alternatively, the repassivation potential has been defined as the potential during cyclic polarization where the forward and reverse scans intersect, a point where the measured current density during the reverse scan drops to a level *known* to be indicative of passivity. Details are discussed in the subsequent section.

The high boron content of $Fe_{49.7}Cr_{17.7}Mn_{1.9}Mo_{7.4}W_{1.6}B_{15.2}C_{3.8}Si_{2.4}$ (SAM2X5) makes it an effective neutron absorber, and suitable for criticality control applications. Average measured values of the neutron absorption cross section in transmission (Σ_t) for Type 316L stainless steel, Alloy C-22, borated stainless steel, a Ni-Cr-Mo-Gd alloy, and SAM2X5 have been determined to be approximately 1.1, 1.3, 2.3, 3.8 and 7.1, respectively, and are discussed in detail in a separate publication.[19] The high boron content of this particular amorphous metal makes it an effective neutron absorber, and suitable for criticality control applications. This material and its parent alloy have been shown to maintain corrosion resistance up to the glass transition temperature, and to remain in the amorphous state after receiving relatively high neutron dose.

II. EXPERIMENTAL

A. Melt Spinning Process

Maximum cooling rates of one million Kelvin per second (10^6 K/s) have been achieved with melt spinning, which is an ideal process for producing amorphous metals over a very broad range of compositions. This process was used to synthesize completely amorphous, Fe-based, corrosion-resistant alloys with near theoretical density, and thereby enabled the effects of coating morphology on corrosion resistance to be separated from the effects of elemental composition. The melt-spun ribbon (MSR) samples prepared with this equipment were several meters long, several millimeters wide and approximately 150 microns thick.

B. Thermal Spray Process

The coatings discussed here were made with the high-velocity oxy-fuel (HVOF) process, which involves a combustion flame, and is characterized by gas and particle velocities that are three to four times the speed of sound (mach 3 to 4). This process is ideal for depositing metal and cermet coatings, which have typical bond strengths of 5,000 to 10,000 pounds per square inch (5-10 ksi), porosities of less than one percent (< 1%) and extreme hardness. The cooling rate that can be achieved in a typical thermal spray process such as HVOF are on the order of ten thousand Kelvin per second (10^4 K/s), and are high enough to enable many alloy compositions to be deposited above their respective critical cooling rate, thereby maintaining the vitreous state. However, the range of amorphous metal compositions that can be processed with HVOF is more restricted than those that can be prepared with melt spinning, due to the differences in achievable cooling rates. Both kerosene and hydrogen have been investigated as fuels in the HVOF process used to deposit SAM2X5. While the thickness of a typical coating ranges from 0.4 to 1.0 mm (nominally 15 to 40 mils), adherent coatings with thicknesses of 7.5 mm have been produced. Free-standing plates with thicknesses as great as 20 mm have also been produced.

C. Energy Dispersive Spectroscopy

The target concentrations of heavier elements such as Cr, Mo and W were verified with Energy Dispersive Spectroscopy (EDS). Microanalysis of each sample was performed at three randomly

selected locations at 10,000X magnification. Compositional analysis was performed on the smoother side of each melt-spun ribbon (MSR), as the rougher sides were found in some cases to be contaminated with trace amounts of copper, presumably from contact with the copper wheel during the melt spinning process. The concentrations of relatively light elements such as B and C could not be determined with EDS, and were therefore estimated with a simple difference calculation, so that the sum of concentrations for all elements totaled one hundred percent.

D. X-Ray Diffraction

The basic theory for X-ray diffraction (XRD) of amorphous materials is well developed and has been published in the literature.[23-24] In the case of amorphous materials, broad peaks are observed. During this study, XRD was done with CuK_{α} X-rays, a crystalline graphite analyzer, and a Philips vertical goniometer, using the Bragg-Bretano method. The X-ray optics were self-focusing, and the distance between the X-ray focal point to the sample position was equal to the distance between the sample position and the receiving slit for the reflection mode. Thus, the intensity and resolution was optimized. Parallel vertical slits were added to improve the scattering signal. Step scanning was performed from 20 to 90° (2θ) with a step size of 0.02° at 4 to 10 seconds per point, depending on the amount of sample. The samples were loaded into low-quartz holder since the expected intensity was very low, thus requiring that the background scattering be minimized.

E. Thermal Analysis

The thermal properties of these Fe-based amorphous metals have also been determined. Thermal analysis of these Fe-based amorphous metals, with differential scanning calorimetry (DSC) or differential thermal analysis (DTA), allowed determination of important thermal properties such as the glass transition temperature (T_g), crystallization temperature (T_x), and the melting point (T_m). Results from the thermal analysis of amorphous samples provided initial assessment of the glass forming ability of these materials through conventional metrics, such as the reduced glass transition temperature ($T_{rg} = T_g/T_L$).

F. Mechanical Properties

Hardness was also measured, since it determined wear resistance, as well as resistance to erosion-corrosion. Vickers micro-hardness (HV) was the standard approach used to assess the hardness of these thermal spray coatings. A 300-gram load was used since it was believed that this load and the affected area were large enough to sample across any existing macro-porosity, thereby producing a spatially averaged measurement. Micro-hardness measurements were also made with a 100-gram load since it was believed that this load and the affected area were small enough to accurately sample bulk material properties.

G. Cyclic Polarization

Cyclic polarization (CP) measurements were based on a procedure similar to ASTM (American Society for Testing and Materials) G-5 and other similar standards, with slight modification.[25-28] The ASTM G-5 standard calls for a 1N H_2SO_4 electrolyte, whereas synthetic bicarbonate, sulfate-chloride, chloride-nitrate, and chloride-nitrate solutions, with sodium, potassium and calcium cations, as well as natural seawater were used for this investigation. The natural seawater used in these tests was obtained directly from Half Moon Bay along the northern coast of California. Furthermore, the ASTM G-5 standard calls for the use of de-aerated

solutions, whereas aerated and de-aerated solutions were used here. In regard to current densities believed to be indicative of passivity, all data was interpreted in a manner consistent with the published literature.[20-22]

Temperature-controlled borosilicate glass (Pyrex) electrochemical cells were used for cyclic polarization and other similar electrochemical measurements. This cell had three electrodes, a working electrode (test specimen), a reference electrode, and a counter electrode. A standard silver silver-chloride electrode, filled with near-saturation potassium chloride solution, was used as the reference, and communicated with the test solution via a Luggin probe placed in close proximity to the working electrode, which minimized Ohmic losses. The electrochemical cell was equipped with a water-cooled junction to maintain reference electrode at ambient temperature, which thereby maintained integrity of the potential measurement, and a water-cooled condenser, which prevented the loss of volatile species from the electrolyte.

To assess the sensitivity of these iron-based amorphous metals to devitrification, which can occur at elevated temperature, melt-spun ribbons of Fe-based amorphous metals were intentionally devitrified by heat treating them at various temperatures for one hour. After heat treatment, the samples were evaluated in low temperature seawater (30°C) with cyclic polarization, to determine the impact of the heat treatment on passive film stability and corrosion resistance. The temperatures used for the heat treatment were: 150, 300, 800 and 1000°C. In general, corrosion resistance was maintained below the crystallization temperature, and lost after prolonged aging at higher temperatures.

H. Potentiostatic Polarization

Potential step tests were used to determine the potential at which the passive film breaks down on $Fe_{49.7}Cr_{17.7}Mn_{1.9}Mo_{7.4}W_{1.6}B_{15.2}C_{3.8}Si_{2.4}$ (SAM2X5) and the reference material, nickel-based Alloy C-22. During prolonged periods of at a constant applied potential, which were typically 24 hours in duration, the current was monitored as a function of time. In cases where passivity was lost, the current increased, and the test sample was aggressively attacked. In cases where passivity was maintained, the current decayed to a relatively constant asymptotic level, consistent with the known passive current density. In these tests, periods of polarization were preceded by one hour at the open circuit corrosion potential (OCP), or rest potential. As a practical matter, increments of applied potential were controlled relative to the initial rest potential. To eliminate the need for surface roughness corrections in the conversion of measured current and electrode area to current density, the SAM2X5 coatings were polished to a 600-grit finish prior to testing. The constant potential denoted in the figures was applied after 1 hour at the OCP.

I. Linear Polarization

The linear polarization method was used as a method for determining the corrosion rates of the various amorphous metal coatings. The procedure used for linear polarization testing consisted of the following steps: (1) holding the sample for ten seconds at the OCP; (2) beginning at a potential 20 mV below the OCP, increasing the potential linearly at a constant rate of 0.1667 mV per second to a potential 20 mV above the OCP; (3) recording the current being passed from the counter electrode to the working electrode as a function of potential relative to a standard Ag/AgCl reference electrode; and (4) determining the parameters in the cathodic Tafel line by performing linear regression on the voltage-current data, from 10 mV below the OCP, to 10 mV above the OCP. The slope of this line was the polarization resistance, *Rp* (ohms), and was

defined in the published literature.[29] While no values for the Tafel parameter (*B*) of Fe-based amorphous metals have yet been developed, it was believed that a conservative value of approximately 25 mV was reasonable, based upon the range of published values for several Fe- and Ni-based alloys.[29] The corrosion current density was then defined in terms of *B*, R_p and *A*, the actual exposed area of the sample being tested. The general corrosion rate was calculated from the corrosion current density through application of Faraday's Law: [30]

$$R_P = \left(\frac{\partial E}{\partial I} \right)_{E_{corr}} \tag{2}$$

The parameter (*B*) was defined in terms of the slopes of the anodic and cathodic branches of the Tafel line:

$$B = \frac{\beta_a \beta_c}{2.303(\beta_a + \beta_c)} \tag{3}$$

Values of B were published for a variety of iron-based alloys, and varied slightly from one alloy-environment combination to another.[29] For example, values for carbon steel, as well as Type 304, 304L and 430 stainless steels, in a variety of electrolytes which include seawater, sodium chloride, and sulfuric acid, ranged from 19 to 25 mV. A value for nickel-based Alloy 600 in lithiated water at 288°C was given as approximately 24 mV. While no values have yet been developed for the Fe-based amorphous metals that are the subject of this investigation, it was believed that a conservative representative value of approximately 25 mV was appropriate for the conversion of polarization resistance to corrosion current. Given the value for Alloy 600, a value of 25 mV was also believed to be acceptable for converting the polarization resistance for nickel-based Alloy C-22 to corrosion current. The corrosion current, I_{corr} (A) was then defined as:

$$I_{corr} = \frac{B}{R_p} \tag{4}$$

where the parameter B was conservatively assumed to be approximately 25 mV. The corrosion current density, i_{corr} (A cm^{-2}), was defined as the corrosion current, normalized by electrode area, and was:

$$i_{corr} = \frac{I_{corr}}{A} \tag{5}$$

where *A* was the surface area of the sample in square centimeters (cm^2). The corrosion (or penetration) rates of the amorphous alloy and reference materials were calculated from the corrosion current densities with the following formula, which is similar to that given by Jones: [30]

$$\frac{dp}{dt} = \frac{i_{corr}}{\rho_{alloy} n_{alloy} F} \tag{6}$$

where p was the penetration depth, t was time, i_{corr} was the corrosion current density, ρ_{alloy} was the density of the alloy (g cm^{-3}), n_{alloy} was the number of gram equivalents per gram of alloy, and F was Faraday's constant. The value of n_{alloy} was calculated with the following formula:

$$n_{alloy} = \sum_j \left(\frac{f_j n_j}{a_j} \right) \tag{7}$$

where f_j was the mass fraction of the j^{th} alloying element in the material, n_j was the number of electrons involved in the anodic dissolution process, which was assumed to be congruent, and a_j was the atomic weight of the j^{th} alloying element. Congruent oxidation or dissolution was assumed, which meant that the dissolution rate of a given alloy element was assumed to be proportional to its concentration in the bulk alloy. These equations were used to calculate factors for the conversion of corrosion current density to the corrosion rate. These conversion factors are summarized in Table II.

J. Junction Potential Correction

It is important to understand the magnitude of the error in the potential measurements due to the junction potential. Consistent with the methods given by Bard and Faulkner, a correction was performed based upon the Henderson Equation.[31] The calculated junction potentials for several test solutions were estimated with ionic properties taken from Bard and Faulkner. These corrections were not very large, with the largest being less than approximately 10 mV. It was therefore concluded that no significant error would result from neglecting the junction potential correction. Some uncertainty and error would have been introduced by using the correction.

K. Salt Fog Testing

Salt fog tests were conducted according to the standard General Motors (GM) salt fog test, identified as GM9540P, or an abbreviation of that test. The protocol for this test is summarized in Table III. Reference samples included 1018 carbon steel, Type 316L stainless steel, nickel-based Alloy C-22, Ti Grade 7, and the 50:50 nickel-chromium binary.

III. EXPERIMENTAL RESULTS

A. Elemental Composition

The compositions of melt-spun ribbons used for this study were verified with EDS and are summarized in Table IV. Melt-spun ribbons were prepared by adding 1, 3, 5 and 7 atomic percent molybdenum to $Fe_{52.3}Mn_2Cr_{19}Mo_{2.5}W_{1.7}B_{16}C_4Si_{2.5}$ (SAM40), and were designated SAM2X1, SAM2X3, SAM2X5 and SAM2X7, respectively. The SAM2X5 ($Fe_{49.7}Cr_{17.7}Mn_{1.9}Mo_{7.4}W_{1.6}B_{15.2}C_{3.8}Si_{2.4}$) provided adequate corrosion resistance, and was a formulation that could be processed with relative ease. The SAM2X7 composition had a higher calculated pitting-resistance equivalence number (PREN) than the alloys with less molybdenum, and slightly better corrosion resistance than SAM2X5, but was somewhat more difficult to make. The PREN is discussed in detail subsequently.

B. Amorphous Structure

Melt-spun ribbons prepared by The NanoSteel Company (TNC) were characterized with XRD. Figure 1a shows the resulting diffraction patterns of melt-spun ribbons of two austenitic alloys,

nickel-based Alloy C-22 and Type 316L stainless steel. These data indicated that both of these materials were indeed crystalline, and that the melt spinning process could not capture the meta-stable glassy state for these compositions. Figure 1b shows X-ray diffraction data for melt-spun ribbon (MSR) samples of iron-based amorphous metals identified as: (a) SAM40; (b) SAM2X1; (c) SAM2X3; (d) SAM2X5; and (e) SAM2X7. These data were indicative of amorphous structure, and a complete lack of crystalline structure, which was attributed to the relatively high concentrations of boron, and a cooling rate above the CCR.

C. Gas Atomized Powders

The absence of crystalline structures was believed to be one factor that contributes to the corrosion resistance of amorphous alloys.[14-16] Residual crystalline structure, mechanical properties, corrosion resistance were assumed to depend upon the distribution of particle sizes in feed powders. A portion of this investigation was directed towards the proof or disproof of this hypothesis. The crystalline structure of powders was found to vary with particle size, since different cooling rates were experienced by particles with different sizes. Particle size sensitivity was explored in regard to the residual crystalline phases present in powders and coatings, as well as in regard to the impact of those crystalline phases on the corrosion resistance of coatings. A correlation has been observed between the formation of substantial amounts of deleterious crystalline phases, such as bcc ferrite, in Fe-based amorphous metals, and the susceptibility to corrosion in chloride-containing environments.[32]

Due to the relatively high critical cooling rate of $Fe_{49.7}Cr_{17.7}Mn_{1.9}Mo_{7.4}W_{1.6}B_{15.2}C_{3.8}Si_{2.4}$ (SAM2X5) in comparison to that of other alloys such as $Fe_{48}Mo_{14}Cr_{15}Y_2C_{15}B_6$ (SAM1651), technological challenges had to be overcome to produce completely amorphous powder with this high-boron Fe-based amorphous metal. It was found that particular care had to be paid to the control of raw materials and conditions within the atomization process. Through careful control of these variables, completely amorphous powders were produced with the SAM2X5 high-boron composition. The particle size distributions of powders typically used as feedstock for HVOF deposition processes usually lie between 15 and 53 microns (–53/+15 μm). To explore the impact of particle size on the residual crystalline content of coatings, as well as the corrosion resistance of these coatings, several particle size distributions were explored. This work therefore provides unique insight into the relationship between particle size, which determines the cooling rate along the radius of the amorphous metal particles, the presence of crystalline phases in the prepared coatings, and the corresponding corrosion resistance.

The corrosion performance of thermal spray coatings of iron-based amorphous metals was found to depend upon the quality of the powder used to produce the coating. In general, completely amorphous powders were required for the deposition of completely amorphous coating, with the desired level of corrosion resistance. Since the powders were softened during thermal spray, and not re-melted, the original degree of crystalline or amorphous structure was preserved. Substantial experience was gained with a wide range of powders having various levels of residual crystalline phase present. Scanning electron microscopy (SEM) of SAM2X5 showed that this powder had spherical morphology, which was essential for good flow characteristics in the thermal spray process (Figure 2).

D. Thermal-Spray Coatings

XRD data for a HVOF coating of SAM2X5 on a nickel-based Alloy C-22 substrate, and deposited with with a JP5000™ thermal-spray gun (Praxair TAFA JP5000 System), is shown in

Figure 3. This coating also had residual crystalline phases present, and was prepared with Lot # 04-265 powder, which had a broad range of particle sizes (–53/+15 μm).

XRD was done on the feed powders prior to coating production. In general, broad halos were observed at 2θ-angles of 44° and 78°, which indicated that SAM2X5 feed powders were predominately amorphous. However, relatively small sharp peaks were also observed, and were attributed primarily to four crystalline phases, including Cr_2B, WC, $M_{23}C_6$ and bcc ferrite.[32] These potentially deleterious precipitates deplete the amorphous matrix of those alloying elements, such as chromium, responsible for enhanced passivity. The largest amount of these crystalline phases was found in Lots # 04-265 (–53/+15 μm) and 04-200 (–53/+30 μm), with relatively little found in Lot # 04-199 (–30/+15 μm). These results are reflected in the XRD data for the coatings produced with each of these powders.

XRD data for a HVOF coating of SAM2X5 on a Type 316L stainless steel substrate, deposited with the JK2000™ thermal spray gun (Deloro Stellite JetKote JK2000 System), is shown in Figure 4. This coating was prepared with Lot # 04-200 powder which had a particle size distribution typical of those used for HVOF processes (–53/+30 μm). XRD data for another HVOF coating of SAM2X5 on a Type 316L stainless steel substrate, deposited with JK2000 thermal spray gun is shown in Figure 5. The coatings with largest amount of Cr_2B, WC, $M_{23}C_6$ and bcc ferrite were prepared with Lots # 04-265 (–53/+15 μm) and 04-200 (–53/+30 μm), while the coating with the least amount of these three crystalline phases was prepared with Lot # 04-199 (–30/+15 μm).

E. Thermal Properties

The thermal properties of these Fe-based amorphous metals have been determined. $Fe_{49.7}Cr_{17.7}Mn_{1.9}Mo_{7.4}W_{1.6}B_{15.2}C_{3.8}Si_{2.4}$ (SAM2X5) had a glass transition temperature of ~579°C, a crystallization temperature of ~628°C, a melting point of ~1133°C, and a reduced glass transition temperature of ~0.57. SAM2X7, an alloy in the same family as SAM2X5, but with more molybdenum, had a glass transition temperature of ~573°C, a crystallization temperature of ~630°C, a melting point of ~1137°C, and a reduced glass transition temperature of 0.57. In contrast, yttrium-containing $Fe_{48}Mo_{14}Cr_{15}Y_2C_{15}B_6$ (SAM1651) had a glass transition temperature of ~584°C, a crystallization temperature of ~653°C, a melting point of ~1121°C, and a reduced glass transition temperature of ~0.55. The critical cooling rates for SAM2X7 and SAM1651 have been determined to be ~610 and ≤ 80 K per second, respectively. Clearly, the yttrium additions in SAM1651 enhanced glass-forming ability of this material. The data for the SAM2X-series of alloys is summarized in Table V.

F. Mechanical Properties

As previously discussed, hardness determines wear resistance, as well as resistance to erosion-corrosion. Vickers micro-hardness (HV) was the standard approach used to assess the hardness of these thermal spray coatings. A 300-gram load was used since it was believed that this load and the affected area were large enough to sample across any existing macro-porosity, thereby producing a spatially averaged measurement. Micro-hardness measurements were also made with a 100-gram load since it was believed that this load and the affected area were small enough to accurately sample bulk material properties. Typical ranges of the measured micro-hardness for these HVOF coatings are summarized in Table VI, and were 1000-1200 for as-sprayed materials,

and were 1200-1500 for devitrified materials. The increase in hardness with devitrification is attributed to the formation of crystalline precipitates.

G. Thermal-Aging Effects

To assess the sensitivity of these iron-based amorphous metals to devitrification, which can occur at very elevated temperature, melt-spun ribbon samples of the parent alloy, $Fe_{52.3}Mn_2Cr_{19}Mo_{2.5}W_{1.7}B_{16}C_4Si_{2.5}$ (SAM40), were intentionally devitrified by aging them at various temperatures for one hour. The temperatures used for the heat treatment were: 150, 300, 800 and 1000°C. Untreated (as received) ribbons were also tested, and provided insight into the baseline performance. As shown in Figure 6, the heat-treated samples were evaluated with in natural seawater at 90°C with cyclic polarization, to determine the impact of the heat treatment on passive film stability and corrosion resistance. These samples showed no significant hysteresis and change in repassivation potential at heat treatments of 150-300°C, but showed a dramatic loss of corrosion resistance when heat treatments were performed at 800-1000°C, which were above the known crystallization temperature of approximately 600-650°C (623°C) given in Table V. Both ribbons treated at elevated temperature showed large hysterisis loops, which were indicative of passive film breakdown, with a clearly defined repassivation potential near -600 mV vs. Ag/AgCl (about 100 mV above the OCP). The operational limit for these materials, when being used for corrosion resistance, appeared to be bounded by the recrystallization temperature.

Melt spun ribbons of $Fe_{49.7}Cr_{17.7}Mn_{1.9}Mo_{7.4}W_{1.6}B_{15.2}C_{3.8}Si_{2.4}$ (SAM2X5) were also intentionally devitrified by heat treating at 800°C for one hour and then subjected to cyclic polarization in 5M $CaCl_2$ at 105°C. In comparison to as-received materials, samples heat-treated at 800°C showed dramatic losses of corrosion resistance. Large hysterisis loops indicative of passive film breakdown, with clearly defined repassivation potentials near the corresponding open-circuit potentials, were observed during cyclic polarization of such heat-treated samples in hot, concentrated calcium chloride solution. Transmission electron microscopy and X-ray diffraction were used to verify the existence of a homogenous amorphous phase below the glass transition temperature. Crystalline precipitates were observed above the crystallization temperature.

H. Passive-Film Stability

Cyclic polarization in natural seawater is shown in Figure 7 at 90°C for two wrought Alloy C-22 samples and a SAM2X5 melt-spun ribbon (MSR). In general, the measured current densities for the SAM2X series of iron-based amorphous-metal melt-spun ribbons were less than those measured for wrought samples of Alloy C-22, which indicated better passivity of the amorphous metals. The anodic oxidation peaks for SAM2X7 and Alloy C-22 are believed to be due to the oxidation of molybdenum within the oxide film.[20]

Cyclic polarization in natural seawater at 90°C is shown in Figure 8 for a wrought Alloy C-22 samples and an as-sprayed high-velocity oxy-fuel (HVOF) coating of SAM2X5, which was deposited on a Type 316L stainless steel substrate. In general, the measured current density for the iron-based amorphous-metal thermal-spray coating in heated seawater was less than those measured for wrought samples of Alloy C-22, indicating better passivity of HVOF SAM2X5 coating in this particular environment. The distinct anodic oxidation peaks for Alloy C-22, and the faint peak for the SAM2X5 thermal spray coating, are all believed to be due to the oxidation of molybdenum.

Potential-step testing in natural seawater heated to 90° was done with: wrought Alloy C-22 (reference material); fully dense and completely amorphous melt spun ribbons of SAM2X5; optimized HVOF coatings prepared with coarse (–53/+30 μm) powders of SAM2X5; and optimized HVOF coatings prepared with relatively fine (–30/+15 μm) powders of SAM2X. These coatings were prepared with SAM2X5 powder supplied by The NanoSteel Company (TNC), and deposited by Plasma Tech Incorporated (PTI) in Torrance, California. Coatings prepared with finer powders were found to have a smaller volume fraction of crystalline precipitates than those prepared with coarser powders. To eliminate the need for surface roughness corrections in the conversion of measured current and electrode area to current density, the SAM2X5 and SAM1651 coatings were polished to a 600-grit finish prior to testing.

Figures 9 through 13 show measured transients in current density at constant applied potentials of 900, 1000, 1100, 1200 and 1400 mV vs. OCP for several different materials in natural seawater at 90°C. The materials compared in each figure include wrought Alloy C-22 (reference material), a fully dense and completely amorphous melt-spun ribbon (MSR) of SAM2X5, HVOF coatings prepared with coarse (–53/+30 μm) powders of SAM2X5, and HVOF coatings prepared with relatively fine (–30/+15 μm) powders of SAM2X5. The constant potential was applied after 1 hour at the open circuit corrosion potential (OCP). The passive film on the melt spun ribbon and HVOF coatings of SAM2X5 were more stable than that on wrought nickel-based Alloy C-22 under these conditions, which lead to the conclusion that this iron-based amorphous metal had superior corrosion resistance.

Transients in current density at a constant applied potential of 900 mV vs. OCP are compared in Figure 9. The periodic current fluctuations (pulses) observed during testing of Alloy C-22 were indicative of the onset of passive film breakdown. The HVOF coating of SAM2X5 prepared with relatively fine (–30/+15 μm) powder had a temporary loss of passivity at 5×10^4 seconds, but underwent repassivation at 8×10^4 seconds. In contrast, the coating prepared with coarse (–53/+30 μm) powder appeared to be completely stable, as did the melt-spun ribbon. The differences in the corrosion resistance of the SAM2X5 coatings prepared with coarse (–53/+30 μm) and relatively fine (–30/+15 μm) powders are not completely understood. Since the coating prepared with the coarser powder had slightly more Cr_2B, WC, $M_{23}C_6$ and bcc ferrite than the coatings produced with the finer powder, the superior passive film stability found with these powders cannot be attributed to the formation of these potentially deleterious crystalline phases. Differences in the interfacial composition, structure and area of individual particles that comprise the coatings may be responsible. The passive film on the melt spun ribbon and HVOF coatings of SAM2X5 prepared with coarse (–53/+30 μm) powder were more stable than that on wrought nickel-based Alloy C-22 under similar conditions, which lead to the conclusion that this iron-based amorphous metal had superior corrosion resistance.

Transients in current density at a constant applied potential of 1000 mV vs. OCP are compared in Figure 10. In this case, the passive films on the melt spun ribbons and HVOF coatings of SAM2X5 were also more stable than that on wrought nickel-based Alloy C-22 under these conditions. Even though fluctuations in current density were observed with coatings prepared with relatively fine powder, the passive films on these amorphous metal samples exhibited greater stability (lower current density) than those on Alloy C-22.

Transients in current density at a constant applied potential of 1100 mV vs. OCP are compared in Figure 11. In this case, the passivity of Alloy C-22 was completely lost, with a dramatic increase in the observed current density to levels between 80 and 90 $\mu A/cm^2$ and dramatic attack of the Alloy C-22. A significant difference was observed between the corrosion resistance of

HVOF SAM2X5 coatings prepared with coarse (–53/+30 μm) and relatively fine (–30/+15 μm) powders, with the coarse powder having better performance. The coating prepared with the fine powder (–30/+15 μm) exhibited fluctuations in current density that are indicative of passive film breakdown at times less than ~2×10^4 seconds, with temporary stabilization, followed by another loss of stability at ~7×10^4 seconds. The coating prepared with the coarse (–53/+30 μm) powder and the melt-spun ribbon both maintained exceptional passivity during the entire test. At 1100 mV vs. OCP, the passive films on the melt spun ribbon and HVOF coatings of SAM2X5 prepared with the coarse powder were found to be more stable than that on wrought nickel-based Alloy C-22, further substantiating the conclusion that this iron-based amorphous metal had superior passive film stability under these conditions.

As the applied potential was increased to 1200 mV vs. OCP, as shown in Figure 12, the Alloy C-22 samples lost all passivity, while the melt-spun ribbons and thermal spray coatings of SAM2X5 maintained passivity. The passivity of coatings prepared with the finer powder stabilized at this high anodic potential. As shown in Figure 13, the passivity of Alloy C-22 was lost at 1400 mV vs. OCP, which was indicated by the current density pulsing to 10 mA/cm^2 followed by decay to 2 mA/cm^2. In contrast, the SAM2X5 samples remained passive, with observed current densities of only 1 to 5 μA/cm^2. The passive film on the melt spun ribbon and HVOF coatings of SAM2X5 was more stable than that on wrought nickel-based Alloy C-22 at 1400 mV vs. OCP.

Current density transients at 100 to 1600 mV vs. OCP, measured with a SAM2X5 melt-spun ribbon in deaerated natural seawater at 90°C, were indicative of good passive film stability, and are shown in Figure 14. The passive film stability of this SAM2X5 sample was maintained at potentials up to 1500 mV vs. OCP, which was approximately 800 mV higher than the critical potential observed with Alloy C-22. At an applied potential of 1600 mV vs. OCP, the passivity of SAM2X5 was lost after several hours.

Current density transients at 100 to 1500 mV vs. OCP, measured with a SAM2X5 thermal-spray coating prepared with relatively fine (–30/+15 μm) powder, in deaerated natural seawater at 90°C, are shown in Figure 15. Current fluctuations (pulses) observed at intermediate potentials were indicative of instability of the passive film. While the passive film appeared to be stable at 1200 mV vs. OCP, current fluctuations were observed as the potential was increased, with a complete loss of passivity at 1500 mV vs. OCP.

Current density transients at 100 to 1500 mV vs. OCP, measured with a SAM2X5 thermal-spray coating prepared with relatively coarse (–53/+30 μm) SAM2X5 powder, in deaerated natural seawater at 90°C, are shown in Figure 16. The passive film stability of this SAM2X5 sample was maintained at potentials up to 1400 mV vs. OCP, which was approximately 700 mV higher than the critical potential observed with Alloy C-22. At an applied potential of 1500 mV vs. OCP, the passivity of SAM2X5 was lost after several hours.

Figure 17 shows a comparison and summary of the data presented in Figures 9 through 16. The asymptotic current density reached after 24 hours at each applied potential (each data point represents a 24 hour test) is plotted for wrought Alloy C-22; fully dense and completely amorphous melt spun ribbons of SAM2X5; HVOF coatings of SAM2X5 prepared with coarse (–53/+30 μm) powder; and HVOF coatings of SAM2X5 prepared with relatively fine (–30/+15 μm) powder. As a practical matter, all data in this figure was plotted as a function of potential relative to the Ag/AgCl reference electrode to enable comparison on a common scale, since each individual sample had its own unique OCP. From this plot of current density vs. potential, it appears that stability of the passive film on wrought Alloy C-22 was maintained at applied

potentials below approximately 250 mV vs. Ag/AgCl, the point at which a dramatic change in slope was observed. Similarly, it was concluded that stabilities of passive films on SAM2X5 thermal spray coatings were maintained at applied potentials below approximately 900 mV vs. Ag/AgCl. The stability of the passive film on the SAM2X5 melt-spun ribbon was maintained at applied potentials below approximately 1200 mV vs. Ag/AgCl. Passive films on the SAM2X5 samples exhibited better stability than those on Alloy C-22. These data enabled a clear and unambiguous determination of the threshold potentials for passive film breakdown in a non-creviced condition.

I. Corrosion Rates

Linear polarization was used to determine the approximate corrosion rates of the thermal spray coatings of SAM2X5 and wrought Alloy C-22 in three relevant environments, natural seawater at two temperature levels, and hot concentrated calcium chloride solution. Linear polarization data for reference alloys and the Fe-based amorphous metals were converted to corrosion rates with the conversion factors given in Table II. Values of the corrosion potential, polarization resistance, corrosion current density, and corrosion rate are summarized in Table VII and Figures 18 through 20. In seawater at both 30 and 90°C, the corrosion rates of HVOF SAM2X5 coatings exhibited slightly lower corrosion rates than either wrought sample of Alloy C-22. The corrosion rates of all materials increased with temperature, as expected. In 5M $CaCl_2$ solution at 105°C, the corrosion rates of HVOF SAM2X5 coatings were comparable to, or slightly lower than that of wrought Alloy C-22. In general, the corrosion rates observed in 5M $CaCl_2$ solution at 105°C were higher than those observed in natural seawater at 30 and 90°C, which was expected.

J. Salt-Fog Performance

Early salt fog testing confirmed the corrosion resistance of the corrosion resistance of thermal spray coatings of SAM2X5 relative to other alloys with less molybdenum. As previously discussed, these coatings were deposited with the high-velocity oxy-fuel (HVOF) process, using amorphous metal powders. HVOF coatings of Type 316L stainless steel and the parent alloy, SAM40, showed significant rusting after only 13 cycles in the GM salt fog test. In contrast, HVOF coatings on nickel-based Alloy C-22 and amorphous SAM2X5 showed no obvious corrosion or rusting after more than 60 cycles. Figure 21 shows several samples coated with SAM2X5, prepared with Lot # 06-015 powder and thermally sprayed with the JK2000 gun using hydrogen fuel, and 1018 carbon steel control (reference) samples, after eight full cycles in the GM salt fog test. No rust was seen on these thermally sprayed amorphous metal coatings, though slight discoloration of was observed on some. In sharp contrast, severe attack of 1018 carbon steel reference samples was observed. It is therefore concluded that these new amorphous metal coatings, prepared with powders have a particle size distribution suitable for HVOF, may provide a good means for protecting less corrosion resistant substrate materials.

IV. DISCUSSION

It has been recognized that the corrosion resistance of both iron- and nickel based crystalline alloys can be enhanced through the additions of Cr, Mo and W for many years.[33-34] These alloying elements are also enhance the corrosion resistance of iron-based amorphous metals. While the pitting resistance equivalence number (PREN) was developed for crystalline alloys, it was used for guidance in determining maximum beneficial elemental concentrations of Cr, Mo

and W used in the materials studied here.[35-40] Initial calculations of the PREN for these amorphous alloys were done using formulae from the published literature.[36]

As pointed out in the literature, an estimate of the relative pitting resistance of alloys can be made using the pitting resistance equivalence number (PREN), which is calculated using the elemental composition of the alloy.[41-46] PREN values for the Fe-based amorphous metals of interest here, and the crystalline reference materials, which include Type 316L stainless steel and Ni-based Alloy C-22, have been calculated using the following equations, and are presented in Table VIII. Equation 8 has been used for estimating the PREN for nickel-based alloys, and accounts for the beneficial effects of Cr, Mo, W and N on corrosion resistance: [41]

$$PREN = [\%Cr] + 3.3 \times [\%Mo + \%W] + 30 \times [\%N] \quad (8)$$

However, this equation was used to predict comparable corrosion resistance for Alloys C-276 and Alloy C-22, while Alloy C-22 was known to be more corrosion resistant. An equation that has been used to make reasonable predictions of the relative corrosion resistance of austenitic stainless steels and nickel-based alloys such as Alloy C-22 is: [42]

$$PREN = [\%Cr] + 3.3 \times \left([\%Mo] + 0.5 \times [\%W]\right) + k \times [\%N] \quad (9)$$

The factor k is an adjustable parameter used to account for the beneficial effects of nitrogen. Reasonable values of the factor k range from 12.8 to 30, with 16 being accepted as a reasonable value.[43] Estimates presented in Table VIII are based on the assumption that the value of k is 16, which has been widely used.[44]

PREN values calculated with Equation 9 indicated that the resistance of the SAM2X5 and SAM1651 amorphous metal formulations should be more resistant to localized corrosion than Type 316L stainless steel or nickel-based Alloy C-22. As in the case of crystalline Fe-based and Ni-based alloys, it was found experimentally that the addition of Cr, Mo, and W substantially increased the corrosion resistance of these amorphous alloys. Additional passive film stability may have been observed, which cannot be attributed to composition alone, and may be attributable to the glassy structure. Additional work is required to further understand the relative roles of composition and crystalline structure in high-performance amorphous metal coatings, such as the ones discussed here.

An obvious deficiency associated with the use of a parameter based on chemical composition alone to assess the relative corrosion resistance of both crystalline and amorphous alloys is that microstructural effects on passive film breakdown are ignored. The lack of crystalline structure is believed to be a key attribute of corrosion resistant amorphous metals.[44]

The effect of powder size on the corrosion performance of Fe-based amorphous metal coatings was studied. Coatings prepared with coarse (-53/+30 μm) powders may have surface features more like fully dense, melt spun ribbons than did coatings prepared with relatively fine (+30/+15 μm) powders. In potential-step experiments with the application of 900, 1000, 1100, 1200, 1300 and 1400 mV vs. OCP, the passive film on coatings prepared with fine (+30/+15 μm) powders exhibited current density transients, which indicated periodic losses of passivity, with intervening periods of repassivation. Such transient were not observed with coatings prepared with coarser (-53/+30 μm) powders. The passive film on nickel-based Alloy C-22 started to destabilize at 900 mV vs. OCP, whereas passive film stability on melt-spun ribbons of SAM2X5 was maintained at an applied potential of 1500 mV vs. OCP, and lost at 1600 mV vs. OCP. In

the case of the thermal spray coatings of SAM2X5 prepared with relatively coarse powder, the passive film maintained stability at 1400 mV vs. OCP, but lost stability at 1500 mV vs. OCP. In the case of the thermal spray coatings of SAM2X5 prepared with the relatively fine powder, the onset of passive film de-stabilization was observed at 900 mV vs. OCP.

The passive film stability observed with coatings prepared with finer particles could be due to any number of phenomena, and deserves further investigation in the future. For example, any residual porosity in the coatings may have behaved like the occluded regions found within a pit or crevice, with lowered pH due to the combined effects of differential aeration, anion transport into the pores, and hydrolysis reactions involving dissolved metal species within the pores, with the production of hydrogen ions. Furthermore, the oxide film covering these occluded surfaces could be more highly defected.

V. CONCLUSIONS

The boron content and corrosion resistance of iron-based amorphous metals may make them attractive candidates for criticality control applications required for the safe long-term storage of spent nuclear fuel.

The hypothesis that the corrosion resistance of iron-based amorphous metals can be enhanced through application of heuristic principles related to the additions of chromium, molybdenum, tungsten has been tested with $Fe_{49.7}Cr_{17.7}Mn_{1.9}Mo_{7.4}W_{1.6}B_{15.2}C_{3.8}Si_{2.4}$ (SAM2X5) and found to have merit. Electrochemical tests show that passive film stability superior to that of Type 316L stainless steel and comparable to that of Alloy C-22 can be achieved iron-based amorphous metals in natural seawater at 30 and 90°C. The passive film on nickel-based Alloy C-22 started to destabilize at approximately 900 mV vs. OCP. The passive films on melt-spun ribbons of SAM2X5 maintained stability at applied potentials greater than 1500 mV vs. OCP, with destabilization observed at 1600 mV vs. OCP.

In general, the corrosion resistance of such iron-based amorphous metals is maintained at operating temperatures up to the glass transition temperature. Thus, the upper operating temperature for such materials was concluded to be about 570°C ($T_g \approx 579$°C). Above the crystallization temperature ($T_x \approx 628$°C), deleterious crystalline phases formed, and the corrosion resistance was lost.

The passive film stability and corrosion resistance found with iron-based amorphous metals depends upon the form being tested. For example, melt-spun ribbons and ingots have been found to have better passive film stability and corrosion resistance than thermal spray coatings. No significant level of Cr_2B, WC, $M_{23}C_6$ and bcc ferrite was detected in the melt spun ribbons, whereas distinct peaks representing these crystalline phases were observed in the XRD of thermal spray coatings.

The effect of powder size on the corrosion performance of Fe-based amorphous metal coatings was studied. The volume fraction of Cr_2B, WC, $M_{23}C_6$ and bcc ferrite in the thermal spray coating depended upon the particle size distribution of the feed powder, but was not the sole determining factor in the relative corrosion resistance of the coatings. In potential-step experiments with the application of 900, 1000, 1100, 1200, 1300 and 1400 mV vs. OCP, the passive film on coatings prepared with relatively fine (+30/+15 μm) powder exhibited current density transients, which indicated periodic losses of passivity, with intervening periods of repassivation. Such transients were not observed with coatings prepared with coarser (-53/+30 μm) powder. Coatings produced with coarse (-53/+30 μm) powder behaved more like the fully dense melt spun ribbon than did the coating produced with relatively fine (+30/+15 μm) powder.

Surprisingly, the coatings produced with the coarse powder, with slightly more Cr_2B, WC, $M_{23}C_6$ and bcc ferrite, had better passive film stability than the coatings produced with relatively fine powder. However, complete devitrification with the formation of much larger concentrations of these precipitates substantially diminishes corrosion resistance.

Thermal spray coatings prepared with early Type 316L stainless steel and the amorphous parent alloy, SAM40, were aggressively attacked during standardized salt fog testing. However, coatings of SAM2X5 prepared with completely amorphous powder showed no corrosion after as many as 60 cycles in standard salt fog tests.

ACKNOWLEDGMENTS

This work was performed by Lawrence Livermore National Laboratory under Contract Number W-7405-Eng-48 and under the auspices of the United States Department of Energy. Work was co-sponsored by the Office of Civilian and Radioactive Waste Management (OCRWM) of the United States Department of Energy (DOE), and the Defense Science Office (DSO) of the Defense Advanced Research Projects Agency (DARPA). The guidance of Jeffrey Walker at DOE OCRWM and Leo Christodoulou at DARPA DSO is gratefully acknowledged. Recent salt-fog testing has been conducted by E-Labs in Fredericksburg, Virginia by Ken Maloy and co-workers. Several substantive scientific comments were provided by Thomas Wolery at LLNL, and served to improve this work.

REFERENCES

1. M. Telford: The case for bulk metallic glass. *Materials Today*, **3,** 36-43 (2004).
2. N. R. Sorensen and R. B. Diegle: Corrosion of amorphous metals. In *Corrosion, Metals Handbook*, 9th Ed., Vol. 13, edited by J. R. Davis and J. D. Destefani (American Society of Metals International, Metals Park, OH, 1987), pp. 864-870.
3. R. M. Latanison: Corrosion resistance of metastable alloys processed by rapid solidification. *Workshop on Amorphous Metals and Semiconductors*, May 12-18, 1985 (Electric Power Research Institute, 1985).
4. D. E. Polk and B. C. Giessen: Overview of principles and applications. Chapter 1, in *Metallic Glasses*, edited by J. J. Gilman and H. J. Leamy (American Society of Metals International, Metals Park, OH, 1978), pp. 2-35.
5. K. Kishitake, H. Era, and F. Otsubo: Characterization of plasma sprayed Fe-10Cr-10Mo-(C,B) amorphous coatings. *J. Thermal Spray Technology*, **5** (2), 145-153 (1996).
6. S. Pang, T. Zhang, K. Asami, and A. Inoue: Effects of chromium on the glass formation and corrosion behavior of bulk glassy Fe-Cr-Mo-C-B alloys. *Materials Transactions*, **43** (8), 2137-2142 (2002).
7. S. J. Pang, T. Zhang, K. Asami, and A. Inoue: Synthesis of Fe-Cr-Mo-C-B-P bulk metallic glasses with high corrosion resistance. *Acta Materialia*, **50**, 489-497 (2002).
8. F. Guo, S. J. Poon, and G. J. Shiflet: Metallic glass ingots based on yttrium. *Metallic Applied Physics Letters*, **83** (13), 2575-2577 (2003).
9. Z. P. Lu, C. T. Liu, and W. D. Porter: Role of yttrium in glass formation of Fe-based bulk metallic glasses. *Metallic Applied Physics Letters*, **83** (13), 2581-2583 (2003).
10. V. Ponnambalam, S. J. Poon, and G. Shiflet: Fe-Mn-Cr-Mo-(Y,Ln)-C-B (Ln=Lanthanides) bulk metallic glasses as formable amorphous steel alloys. *J. Materials Research*, **19** (5), 1320, 2004.

11. J. C. Farmer, J. J. Haslam, S. D. Day, D. J. Branagan, C. A. Blue, J. D. K. Rivard, L. F. Aprigliano, N. Yang, J. H. Perepezko, and M. B. Beardsley: Paper PVP2005-71664, Pressure Vessels and Piping Division Conference, Denver, CO, July 17-21, 2005 (American Society of Mechanical Engineers, Three Park Avenue, New York, NY, 2005).
12. J. C. Farmer, J. J. Haslam, S. D. Day, T. Lian, R. Rebak, N. Yang, and L. Aprigliano: Corrosion resistance of iron-based amorphous metal coatings. Paper PVP2006-ICPVT11-93835, *Pressure Vessels and Piping Division Conference*, Vancouver, BC, July 23-27, 2006 (American Society of Mechanical Engineers, Three Park Avenue, New York, NY, 2006).
13. H. Shinimiya, A. Nakazawa, Z. Kato, A. A. El Moneium, Y. Niizeki, K. Asami, and K. Hashimoto: Corrosion resistant bulk amorphous Ni-Cr-Ta-Mo-Nb-5P alloys in concentrated hydrochloric acids. Paper 319, *Session on Corrosion and Electrochemistry of Advanced Materials in Honor of Koji Hashimoto*, 208th Meeting of the Electrochemical Society, Westing Bonaventure Hotel, Los Angeles, California, October 16-21, 2005 (Electrochemical Society, Pennington, NJ, 2005).
14. D. Chidambaram, C. R. Clayton, and M. R. Dorfman: Evaluation of the electrochemical behavior of HVOF-sprayed alloy coatings. *Surface and Coatings Technology*, **176**, 307-317 (2004).
15. D. J. Branagan, Method of modifying iron-based glasses to increase crystallization temperature without changing melting temperature. U.S. Patent Application No. 20040250929, Filed Dec. 16, 2004.
16. D. J. Branagan: Properties of amorphous/partially crystalline coatings. U.S. Patent Application No. 20040253381, Filed Dec. 16, 2004.
17. J. Farmer, J. Haslam, S. Day, T. Lian, C. Saw, P. Hailey, J-S. Choi, R. Rebak, N. Yang, R. Bayles, L. Aprigliano, J. Payer, J. Perepezko, K. Hildal, E. Lavernia, L. Ajdelsztajn, D. J. Branagan, and M. B. Beardsely: A high-performance corrosion-resistant iron-based amorphous metal – the effects of composition, structure and environment on corrosion resistance. *Scientific Basis for Nuclear Waste Management XXX*, Symposium NN, Boston, MA, Nov. 27 – Dec. 1, 2006 (Materials Research Society, 2006).
18. T. Lian, D. Day, P. Hailey, J-S. Choi, and J. Farmer: Comparative study on the corrosion resistance of Fe-based amorphous metal, borated stainless steel and Ni-Cr-Mo-Gd alloy. Scientific Basis for Nuclear Waste Management XXX, Symposium NN, Boston, MA, Nov. 27 – Dec. 1, 2006 (Materials Research Society, 2006).
19. J-S. Choi, C. Lee, J. Farmer, D. Day, M. Wall, C. Saw, M. Boussoufi, B. Liu, H. Egbert, D. Branagan, and A. D'Amato: Application of neutron-absorbing structural amorphous metal coatings for spent nuclear fuel container to enhance criticality safety controls. Scientific Basis for Nuclear Waste Management XXX, Symposium NN, Boston, MA, Nov. 27 – Dec. 1, 2006 (Materials Research Society, 2006).
20. J. Farmer, S. Lu, D. McCright, G. Gdowski, F. Wang, T. Summers, P. Bedrossian, J. Horn, T. Lian, J. Estill, A. Lingenfelter, and W. Halsey: General and localized corrosion of high-level waste container in Yucca Mountain. Pressure Vessel and Piping Conference, Seattle, WA, July 23-27, 2000, In *Transportation, Storage, and Disposal of Radioactive Materials*, PVP Vol. 408 (American Society of Mechanical Engineers, Three Park Avenue, New York, NY, 2000), pp. 53-70.
21. J. R. Scully, J. L. Hudson, T. Lunt, G. Ilevbare, and B. Kehler: Localized corrosion initiation and transition to stabilization in alloys 625 and C-22. Final Report, TRW/DOE Yucca

Mountain Project Purchase Order No. A10762JM8A (University of Virginia, Charlottesville, VA, Sep. 30, 1999).
22. K. A. Gruss, G. A. Cragnolino, D. S. Dunn, and N. Sridar: Repassivation potential for localized corrosion of alloys 625 and C22 in simulated repository environments. Paper 149, *Corrosion 98* (National Association of Corrosion Engineers International, Houston, TX, 1998).
23. C. K. Saw: In *X-ray Scattering Techniques for Characterization Tools in the Life Sciences, Nanotechnologies for the Life Science*, edited by Challa Kumar (Wiley-VCH Verlag GmbH and Company, KGaA, Weinheim, 2006).
24. C. K. Saw and R. B. Schwarz: Chemical short-range order in dense random-packed models. *J. Less-Common Metals*, **140**, 385-393 (1988).
25. Standard reference test method for making potentiostatic and potentiodynamic anodic polarization measurements. Designation G 5-94, In *1997 Annual Book of American Society for Testing and Materials Standards,* Section 3, Vol. 3.02 (American Society for Testing and Materials, 1997), pp. 54–57.
26. Standard reference test method for making potentiostatic and potentiodynamic anodic polarization measurements. Designation G 5-87, In *1989 Annual Book of American Society for Testing and Materials Standards*, Section 3, Vol. 3.02 (American Society for Testing and Materials, 1989), pp. 79–85.
27. Standard practice for conventions applicable to electrochemical measurements in corrosion testing. Designation G 3-89, In *1997 Annual Book of American Society for Testing and Materials Standards*, Section 3, Vol. 3.02, (American Society for Testing and Materials, 1997), pp. 36–44.
28. Standard test method for conducting cyclic potentiodynamic polarization measurements for localized corrosion susceptibility of iron-, nickel-, or cobalt-based alloys. Designation G 61-86, In 1997 Annual Book of American Society for Testing and Materials Standards, Section 3, Vol. 3.02 (American Society for Testing and Materials, 1997), pp. 231–235.
29. R. S. Treseder, R. Baboian, and C. G. Munger: Polarization resistance method for determining corrosion rates. In *Corrosion Engineer's Reference Book*, 2nd Ed. (National Association of Corrosion Engineers International, Houston, TX, 1991), pp. 65-66.
30. D. A. Jones: Electrochemical kinetics of corrosion – Faraday's law. Chapter 3, in *Principles and Prevention of Corrosion*, 2nd Ed., Section 3.1.1, Equations 3-5 (Prentice Hall, Upper Saddle River, NJ, 1996), pp. 75–76.
31. A. J. Bard and L. R. Faulkner: Potentials and thermodynamics of cells – liquid junction potentials. Chapter 2, in *Electrochemical Methods, Fundamentals and Applications*, Section 2.3, Table 2.3.2, Equation 2.3.39 (John Wiley and Sons, New York, NY, 1980), p. 67, 71.
32. N. Yang, J. Yio, J. Chames, M. Clift, A. Gardea, G. Lucadamo, D. Day, J. Farmer and J. Boudreau: *Microstructure Comparison of SAM2X5 feedstock powder delivered by TNC in FY2004 and FY2005 for HPCRM program*. SAND2006-2490 (Sandia National Laboratory, Livermore, CA, 2006) 26 pages.
33. H. P. Hack: Crevice corrosion behavior of molybdenum-containing stainless steel in seawater. *Materials Performance*, **22** (6) 24–30 (1983).
34. A. I. Asphahani: Corrosion resistance of high performance alloys. *Materials Performance*, **19** (12) 33–43 (1980).
35. J. C. Farmer et al.: High-performance corrosion-resistant amorphous metals. *Global 2003*, New Orleans, LA, 2003 (American Nuclear Society, 2003).

36. D. J. Branagan, M. C. Marshall, and B. E. Meacham: High performance corrosion resistant materials for naval warfighting and safe long-term storage/disposal of spent nuclear fuel. *Final Report*, LLNL Subcontract, LLNL-RFP-B550033 (Institute of Nanomaterials Research and Development, The NanoSteel Company, Idaho Falls, ID, 2005) 84 pages.
37. J. Farmer, C. Earl, C. Doty, D. Spence, J. Walker, F. Wong, J. Payer, G-Q. Lu, D. E. Clark, D. C. Folz, A. Heuer, O. Graeve, D. Branagan, C. Blue, J. Rivard, J. Perepezko, L. Kaufman, N. Yang, E. Lavernia, J. Haslam, E. Lemieux, L. Aprigliano, B. Beardsley, T. Weaver, B. Edwards, B. Brown, A. Halter, B Bayles and J. Lewandowski: *DARPA-DOE High Performance Corrosion-Resistant Materials Principal Investigator's Meeting*, Turtle Bay Resort, Oahu, Hawaii, January 10-13, 2005, UCRL-PRES-214672 (Lawrence Livermore National Laboratory, Livermore, CA, 2005), 407 pages.
38. J. C. Farmer, J. J. Haslam and S. D. Day: High-performance corrosion-resistant iron-based amorphous-metal coatings – evaluation of corrosion resistance. *HPCRM Annual Report*, UCRL-SR-218144 (Lawrence Livermore National Laboratory, Livermore, CA, 2006), 68 pages.
39. J. C. Farmer, J-S. Choi, J. J. Haslam, S. D. Day, N. Yang, T. Headley, G. Lucadamo, J. L Yio, J. Chames, A. Gardea, M. Clift, C. A. Blue, W. H. Peters, J. D. K. Rivard, D. C. Harper, D. Swank, R. Bayles & E. J. Lemieux, Robert Brown & Theresa M. Wolejsza, L. F. Aprigliano, D. J. Branagan, M. C. Marshall, Brian E. Meacham, E. Joseph Buffa, M. Brad Beardsley, E. J. Lavernia, J. Schoenung, L. Ajdelsztajn, J. Dannenberg, O. A. Graeve, J. J. Lewandowski, John H. Perepezko, Kjetil Hildal, L. P. Kaufman, J. Boudreau: High-performance corrosion-resistant iron-based amorphous metal coatings. *Team FY05 HPCRM Annual Report*, UCRL-SR-219257 (Lawrence Livermore National Laboratory, Livermore, CA, 2006), 138 pages.
40. J. Farmer, J. Haslam, S. Day, T. Lian, C. Saw, P. Hailey, J-S. Choi, N. Yang, C. Blue, W. Peter, R. Bayles, R. Brown, J. Payer, J. Perepezko, K. Hildal, E. Lavernia, L. Ajdelsztajn, D. J. Branagan, J. Buffa, M. Beardsley, L. Aprigliano and J. Boudreau: Corrosion resistance of iron-based amorphous metals in hot concentrated calcium chloride and seawater: $Fe_{48}Mo_{714}Cr_{15}Y_2C_{15}B_6$. UCRL-TM-224159 (Lawrence Livermore National Laboratory, Livermore, CA, Aug. 30, 2006), 47 pages.
41. R. B. Rebak and P. Crook: Improved pitting and crevice corrosion resistance of nickel and cobalt based alloys. In *Proc. Symposium on Critical Factors in Localized Corrosion III*, 194th Meeting of the Electrochemical Society, Boston, Massachusetts, November 1-6, 1998, Vol. 98-17 (The Electrochemical Society, Pennington, NJ, 1999), pp. 289-302.
42. Z. Szklarska-Smialowska: Pitting resistance equivalence number, effect of alloying elements on stainless steels and Ni-base alloys. Chapter 13, in *Pitting and Crevice Corrosion* (National Association of Corrosion Engineers International, Houston, TX, 2005), p. 318-321.
43. 4. A. J. Sedriks: Introduction, pitting. Chapter 4, in *Corrosion of Stainless Steels* (J. Wiley & Sons, Inc., New York, NY, 1996), p. 111-113.
44. Pitting corrosion. (www.corrosion-doctors.org/localized/pitting.htm, Dec. 23, 2006).
45. D. C. Agarwal and M. Kohler: Alloy 33, a new material resisting marine environment. Paper 424, *Corrosion 97* (National Association of Corrosion Engineers International, Houston, TX 1997).
46. C. Thornton and C. Cooper: Overmatching superalloy consumable Inco-weld, 686CPT broadens its applications to include welding super austenitic and super duplex stainless steels. In *Stainless Steel World* (KCI Publishing BV 1, 2004).

TABLES

Table I – The melt-spinning process was used to perform a systematic study of various elemental compositions, each based on the Fe-based DAR40 composition, with 1, 3, 5, and 7 atomic percent additions of specific elements believed to be beneficial to glass formation or corrosion resistance. Elemental additions investigated included nickel (Ni), molybdenum (Mo), yttrium (Y), titanium (Ti), zirconium (Zr) and chromium (Cr). The two formulations of greatest interest at the present time, based upon corrosion resistance and ease of processing are SAM2X5 ($Fe_{49.7}Cr_{17.7}Mn_{1.9}Mo_{7.4}W_{1.6}B_{15.2}C_{3.8}Si_{2.4}$), which has a relatively high CCR, and yttrium-containing SAM1651 ($Fe_{48.0}Cr_{15.0}Mo_{14.0}B_{6.0}C_{15.0}Y_{2.0}$), which has a relatively low CCR.

Target Compositions in Atomic Percent - Used to Prepare Samples														
Alloy	Specification / Formula	Fe	Cr	Mn	Mo	W	B*	C*	Si	Y	Ni	P*	Co	Total
Type 316L	UNS S31603	68.0	18.0	1.5	1.5	0.0	0.0	0.0	1.0	0.0	10.0	0.0	0.0	100
Alloy C-22	UNS N06022	4.0	25.0	0.1	8.0	1.4	0.0	0.0	1.0	0.0	60.0	0.0	0.5	100
SAM40	$Fe_{52.3}Mn_2Cr_{19}Mo_{2.5}W_{1.7}B_{16}C_4Si_{2.5}$	52.3	19.0	2.0	2.5	1.7	16.0	4.0	2.5	0.0	0.0	0.0	0.0	100
SAM2X1	$(SAM40)_{99} + Mo_1$	51.8	18.8	2.0	3.5	1.7	15.8	4.0	2.5	0.0	0.0	0.0	0.0	100
SAM2X3	$(SAM40)_{97} + Mo_3$	50.7	18.4	1.9	5.4	1.6	15.5	3.9	2.4	0.0	0.0	0.0	0.0	100
SAM2X5	$(SAM40)_{95} + Mo_5$	49.7	18.1	1.9	7.4	1.6	15.2	3.8	2.4	0.0	0.0	0.0	0.0	100
SAM2X7	$(SAM40)_{93} + Mo_7$	48.6	17.7	1.9	9.3	1.6	14.9	3.7	2.3	0.0	0.0	0.0	0.0	100
SAM1651	$Fe_{48}Mo_{14}Cr_{15}Y_2C_{15}B_6$	48.0	15.0	0.0	14.0	0.0	6.0	15.0	0.0	2.0	0.0	0.0	0.0	100

Table II – The conversion of the corrosion current density to penetration rate (corrosion rate) requires the parameters summarized in this table. These penetration rates are for an assumed current density of one microamp per square centimeter (1 μA cm^{-2}). If the corrosion rate is 2 μA cm^{-2} instead of the assumed 1 μA cm^{-2}, the penetration rate is simply doubled. The value of Faraday's constant (F) is 96,484.6 C $equiv^{-1}$.

Alloy	ρ_{alloy}	$n_{alloy} = (f_j n_j / a_j)/100$		$(dp/dt) = (i_{corr})/(\rho_{alloy} \times n_{alloy} \times F)$			
	g cm^{-3}			cm sec^{-1}		μm $year^{-1}$	
		Low	High	Low	High	Low	High
Type 316L	7.85	3.90×10^{-2}	6.53×10^{-2}	2.02×10^{-11}	3.38×10^{-11}	6.38	10.7
Alloy C-22	8.69	3.80×10^{-2}	6.75×10^{-2}	1.77×10^{-11}	3.14×10^{-11}	5.57	9.89
SAM2X5	7.65	5.41×10^{-2}	7.93×10^{-2}	1.71×10^{-11}	2.50×10^{-11}	5.39	7.89
SAM1651	6.18	4.70×10^{-2}	8.02×10^{-2}	2.09×10^{-11}	3.57×10^{-11}	6.59	11.3

Table III – A description of the standard GM9540P Salt Fog Test is summarized here. Note that the salt solution mists (denoted with asterisks) consisted of 1.25% solution containing 0.9% sodium chloride, 0.1% calcium chloride, and 0.25% sodium bicarbonate.

24-Hour Test Cycle for GM9540P Accelerated Corrosion Test		
Shift	Elapsed Time (hrs)	Event
Ambient Soak	0	Salt solution mist for 30 seconds, followed by ambient exposure at 13-28°C (55-82°F)
	1.5	Salt solution mist for 30 seconds, followed by ambient exposure at 13-28°C (55-82°F)
	3	Salt solution mist for 30 seconds, followed by ambient exposure at 13-28°C (55-82°F)
	4.5	Salt solution mist for 30 seconds, followed by ambient exposure at 13-28°C (55-82°F)
Wet Soak	8 to 16	High humidity exposure for 8 hours at 49 ± 0.5°C (120 ± 1°F) and 100% RH, including a 55-minute ramp to wet conditions
Dry Soak	16 to 24	Elevated dry exposure for 8 hours at 60 ± 0.5°C (140 ± 1°F) and less than 30% RH, including a 175-minute ramp to dry conditions

Table IV – The concentrations of heavy elements used in samples of Type 316L stainless steel, Alloy C-22, SAM40, SAM2X1, SAM2X3, SAM2X5, SAM2X7 and SAM1651 used in this study were verified with energy dispersive X-ray spectroscopy (EDS). Data for melt-spun ribbons of SAM2X40, SAM40, SAM2X1, SAM2X3, SAM2X5 and SAM2X7 and a drop-cast ingot of SAM1651 are presented in this table.

Actual Compositions in Atomic Percent - Determined by Energy Dispersive X-Ray Spectroscopy														
Alloy	Sample	Fe	Cr	Mn	Mo	W	B*	C*	Si	Y	Ni	P*	Co	Total
Type 316L	MSR	67.6	18.7	1.3	1.2	0.0	0.0	0.0	1.2	0.0	10.0	0.0	0.0	100
Alloy C-22	MSR	3.9	25.2	0.1	7.8	1.4	0.0	0.0	1.1	0.0	60.0	0.0	0.5	100
SAM40	MSR	51.9	19.2	2.6	2.5	1.5	16.0	4.0	2.2	0.0	0.0	0.0	0.0	100
SAM2X1	MSR	52.0	19.1	2.7	2.9	1.6	15.8	4.0	1.9	0.0	0.0	0.0	0.0	100
SAM2X3	MSR	49.3	17.9	2.6	5.3	2.5	15.5	3.8	3.1	0.0	0.0	0.0	0.0	100
SAM2X5	MSR	48.8	17.6	2.4	7.2	2.5	15.0	3.7	2.7	0.0	0.0	0.0	0.0	100
SAM2X7	MSR	46.9	16.9	2.3	10.0	2.5	14.9	3.7	2.9	0.0	0.0	0.0	0.0	100
SAM1651	Ingot	49.1	14.6	0.0	13.9	0.0	5.9	14.0	0.3	1.9	0.2	0.0	0.0	100

** The concentrations of relatively light elements such as B and C could not be determined with EDS, and were therefore estimated with a simple difference calculation, so that the sum of concentrations for all elements totaled one hundred percent.*

Table V – Thermal analysis data (DTA or DSC) for Fe-based glass forming alloys suitable for thermal spray deposition as summarized in this table. The two formulations of greatest interest at the present time are SAM2X5 ($Fe_{49.7}Cr_{17.7}Mn_{1.9}Mo_{7.4}W_{1.6}B_{15.2}C_{3.8}Si_{2.4}$), which has a relatively high CCR, and yttrium-containing SAM1651 ($Fe_{48.0}Cr_{15.0}Mo_{14.0}B_{6.0}C_{15.0}Y_{2.0}$), which has a relatively low CCR. These selections are based upon their good corrosion resistance and relative ease or processing.

Alloy	T_g (°C)	T_x (°C)	T_m (°C)	T_L (°C)	T_{rg}
SAM40	568-574	623	1110	1338	0.53
SAM2X1	575	620	1124	1190-1210	0.57
SAM2X3	578	626	1131	1190-1210	0.57
SAM2X5	579	628	1133	1190-1210	0.57
SAM2X7	573	630	1137	1190-1210	0.57
SAM1651	584	653	1121	1290	0.55

Table VI – Measurements of the micro-hardness of Fe-based amorphous metal thermal spray coatings.

	Measured Vickers Micro-Hardness (kg mm^{-2})	
Loading Conditions	As-Sprayed HVOF-Coating	Devitrified at 700°C for 10 Minutes
HV100 (100-gram load)	1050-1200	1300-1500
HV300 (300-gram load)	1000-1100	1200-1350

Table VII – Values of the polarization resistance, corrosion current density, and corrosion rate, measured with linear polarization, are summarized for HVOF coatings of SAM2X5 and Alloy C-22, as well as wrought samples of Alloy C-22.

Sample	Identification	Parameter	E_{corr}	R_p	i_{corr}	dp/dt
			mV	ohms cm²	A/cm²	µm/yr
30°C Seawater						
HVOF SAM2X5	E316L443	Average	-87	$1.63\times10^{+6}$	2.27×10^{-8}	0.18
		Standard Deviation	5.7	$1.37\times10^{+6}$	1.36×10^{-8}	0.11
Wrought Alloy C-22	JE1589	Average	-163	$2.74\times10^{+6}$	9.12×10^{-9}	0.09
		Standard Deviation	1.5	$9.13\times10^{+4}$	3.02×10^{-10}	< 0.01
Wrought Alloy C-22	CC-22 4000	Average	-312	$6.23\times10^{+7}$	5.07×10^{-9}	0.05
		Standard Deviation	3.0	$1.02\times10^{+8}$	4.40×10^{-9}	0.04
90°C Seawater						
HVOF SAM2X5	E316L442	Average	-241	$1.26\times10^{+5}$	2.00×10^{-7}	1.58
		Standard Deviation	7.2	$1.04\times10^{+4}$	1.73×10^{-8}	0.14
Wrought Alloy C-22	JE1594	Average	-319	$7.69\times10^{+4}$	3.25×10^{-7}	3.22
		Standard Deviation	0.8	$4.95\times10^{+2}$	2.10×10^{-9}	0.02
Wrought Alloy C-22	CC-22 4002 # 1	Average	-340	$7.73\times10^{+4}$	3.24×10^{-7}	3.20
		Standard Deviation	0.2	$1.03\times10^{+3}$	4.29×10^{-9}	0.04
Wrought Alloy C-22	CC-22 4002 # 2	Average	-318	$2.03\times10^{+5}$	1.23×10^{-7}	1.22
		Standard Deviation	0.7	$9.07\times10^{+2}$	5.50×10^{-10}	< 0.01
105°C 5M $CaCl_2$						
HVOF SAM2X5	E316L456	Average	-241	$7.32\times10^{+4}$	3.42×10^{-7}	2.70
		Standard Deviation	1.8	$1.03\times10^{+3}$	4.76×10^{-9}	0.04
Wrought Alloy C-22	CC-22 4009	Average	-464	$4.93\times10^{+4}$	5.10×10^{-7}	5.04
		Standard Deviation	3.0	$4.14\times10^{+3}$	4.37×10^{-8}	0.43
HVOF Alloy C-22	E316L235	Average	-348	$2.14\times10^{+3}$	1.17×10^{-5}	116
		Standard Deviation	4.5	$8.94\times10^{+1}$	4.82×10^{-7}	< 5

Table VIII – Values of the pitting resistance equivalence number (PREN) for reference alloys and Fe-based amorphous metals.

Alloy	Low	Ave	High
316L	23	26	30
C-22	65	71	76
SAM2X5	66	74	90
SAM1651	96	100	103

FIGURES

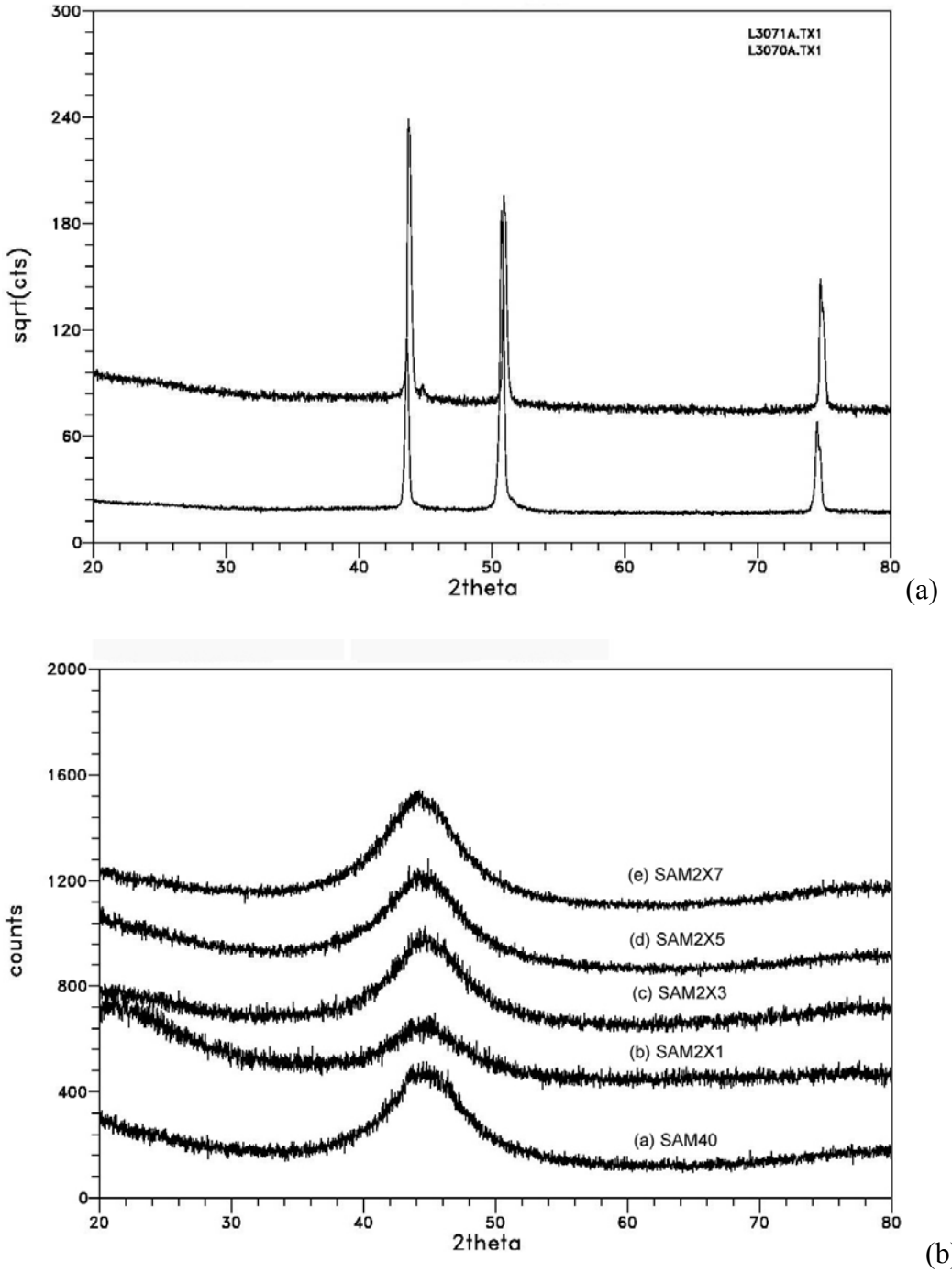

Fig. 1 – (a) This figure shows X-ray diffraction data for melt-spun ribbon (MSR) samples of Type 316L stainless steel and nickel-based Alloy C-22. The strong peaks are indicative of the crystalline nature of these materials. (b) This figure shows X-ray diffraction data for melt-spun ribbon (MSR) samples of iron-based amorphous metals identified as: (a) SAM40; (b) SAM2X1; (c) SAM2X3; (d) SAM2X5; and (e) SAM2X7. All ribbons were completely amorphous.

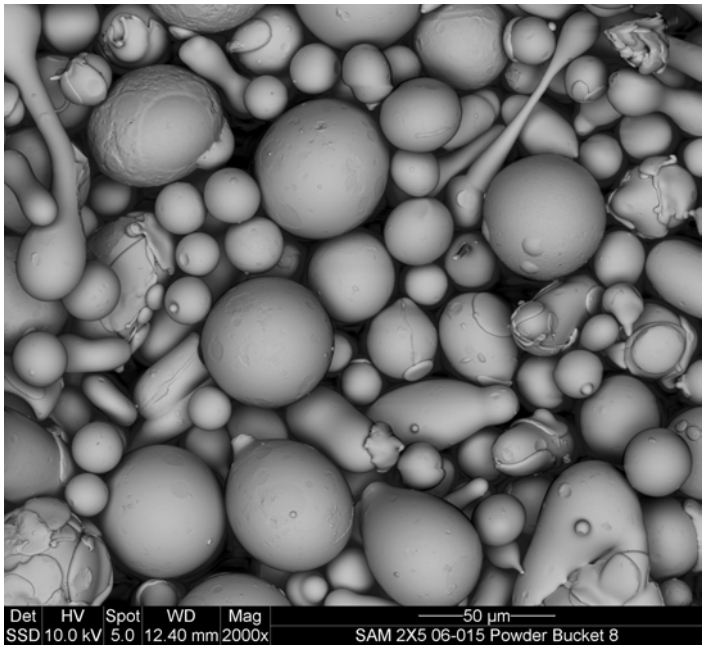

Fig. 2 – Electron micrographs are shown for SAM2X5 Lot # 06-123 powder. This powder has predominantly spherical morphology, which is essential for good flow characteristics in thermal spray processes.

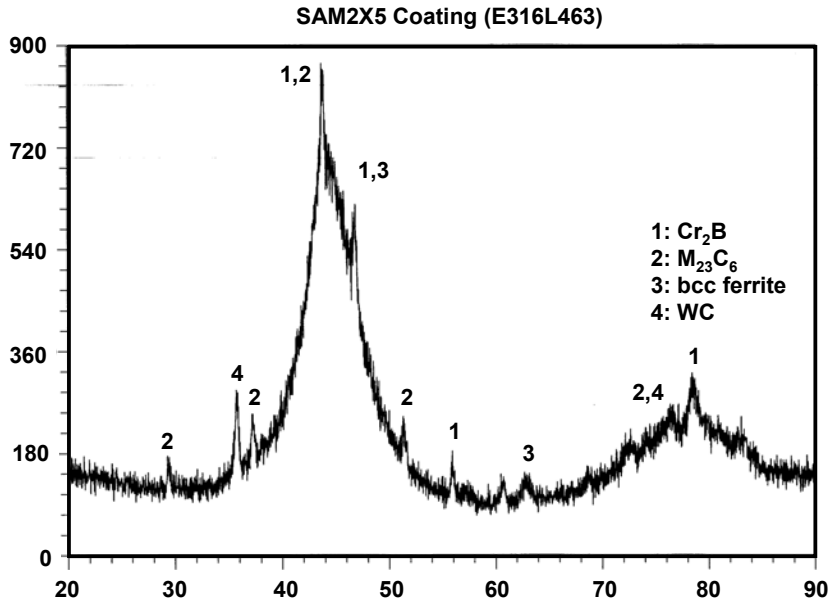

Fig. 3 – XRD data (intensity vs. diffraction angle 2θ) for high-velocity oxy-fuel (HVOF) coating of $Fe_{49.7}Cr_{17.7}Mn_{1.9}Mo_{7.4}W_{1.6}B_{15.2}C_{3.8}Si_{2.4}$ (SAM2X5) on Type 316L stainless steel substrate prepared with JP5000 thermal spray gun. This coating, identified as E316L463, was prepared with Lot #04-265 powder, which had a broad range of particle sizes (–53/+15µm).

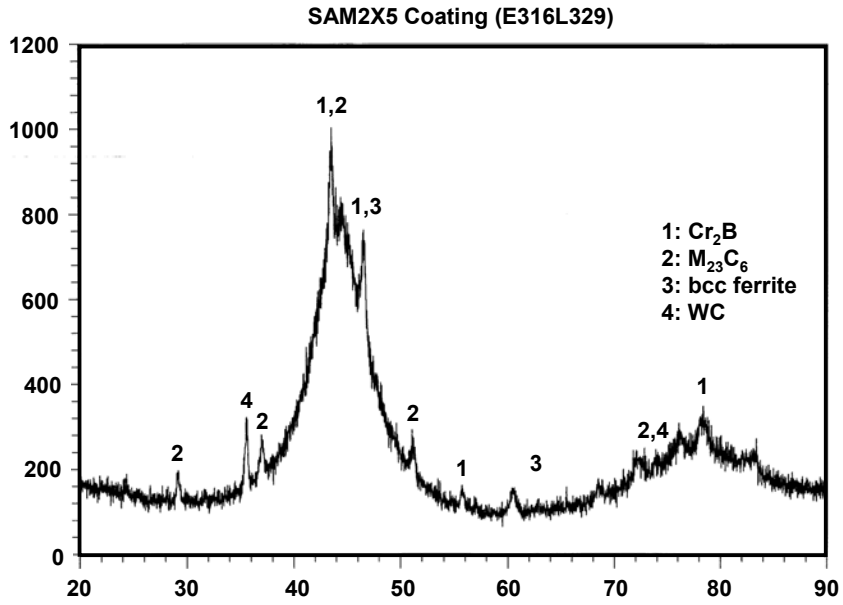

Fig. 4 – XRD data (intensity vs. diffraction angle 2θ) for high-velocity oxy-fuel (HVOF) coating of $Fe_{49.7}Cr_{17.7}Mn_{1.9}Mo_{7.4}W_{1.6}B_{15.2}C_{3.8}Si_{2.4}$ (SAM2X5) on a Type 316L stainless steel substrate, and deposited with a JK2000 thermal-spray gun at Plasma Tech Incorporated (PTI). This coating, identified as E316L329, was prepared with Lot # 04-200 powder, which had a relatively coarse range of particle sizes (–53/+30μm).

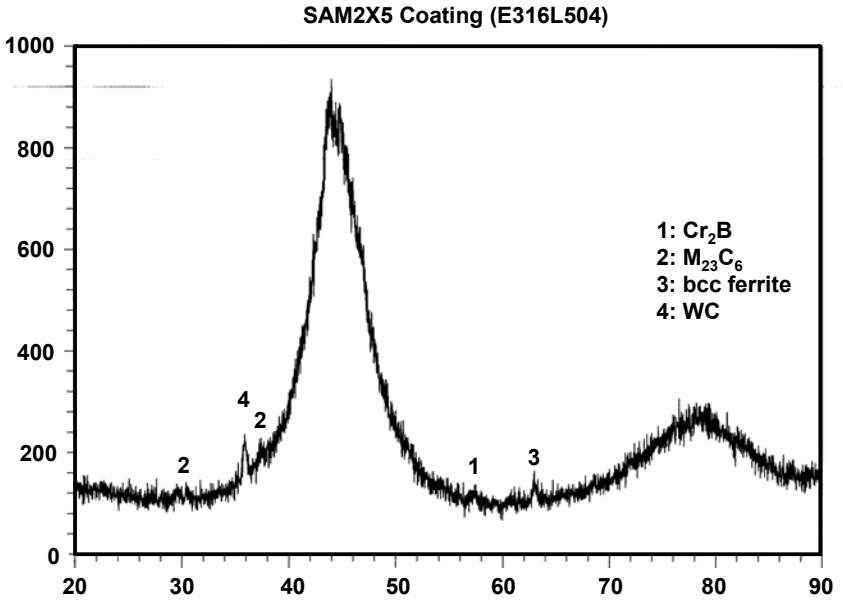

Fig. 5 – XRD data (intensity vs. diffraction angle 2θ) for high-velocity oxy-fuel (HVOF) coating of SAM2X5 on a Type 316L stainless steel substrate, deposited with a JK2000 thermal-spray gun at Plasma Tech Incorporated (PTI). This coating, identified as E316L504, was prepared with Lot # 04-199 powder, which had a relatively fine range of particle sizes (–30/+15μm), and is a standard size distribution for HVOF applications.

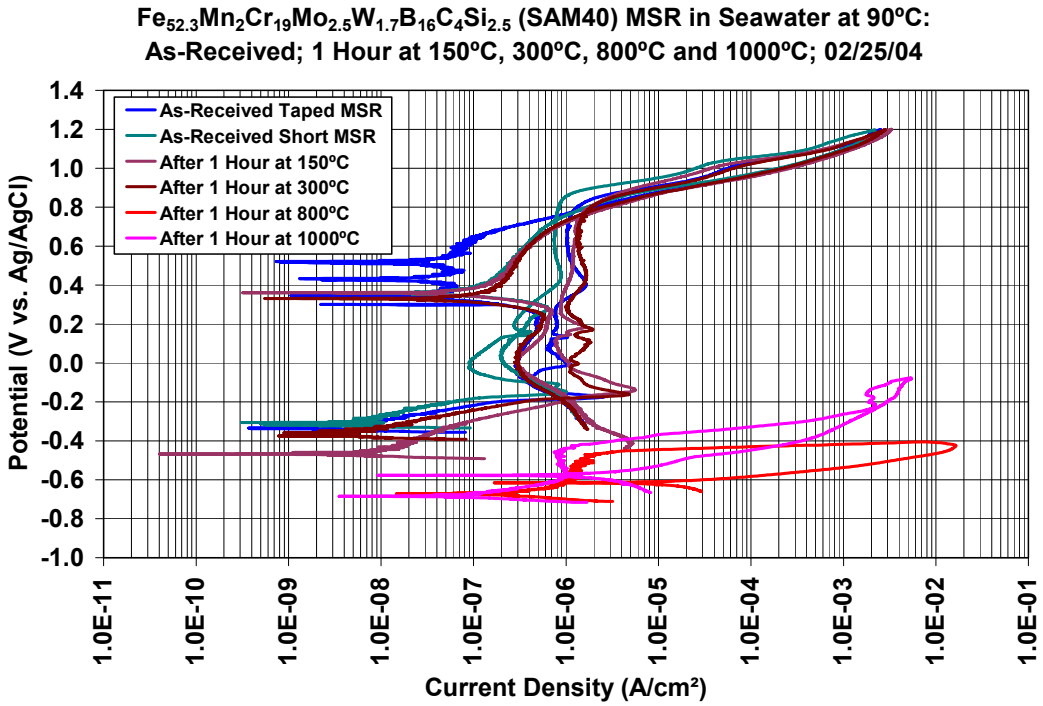

Fig. 6 – Cyclic polarization of melt-spun ribbons of $Fe_{52.3}Mn_2Cr_{19}Mo_{2.5}W_{1.7}B_{16}C_4Si_{2.5}$ (SAM40), were intentionally devitrified by heat treating them at various temperatures for one hour, in natural seawater at 90°C, to determine the impact of the heat treatment on passive film stability and corrosion resistance. The temperatures used for the heat treatment were: 150, 300, 800 and 1000°C.

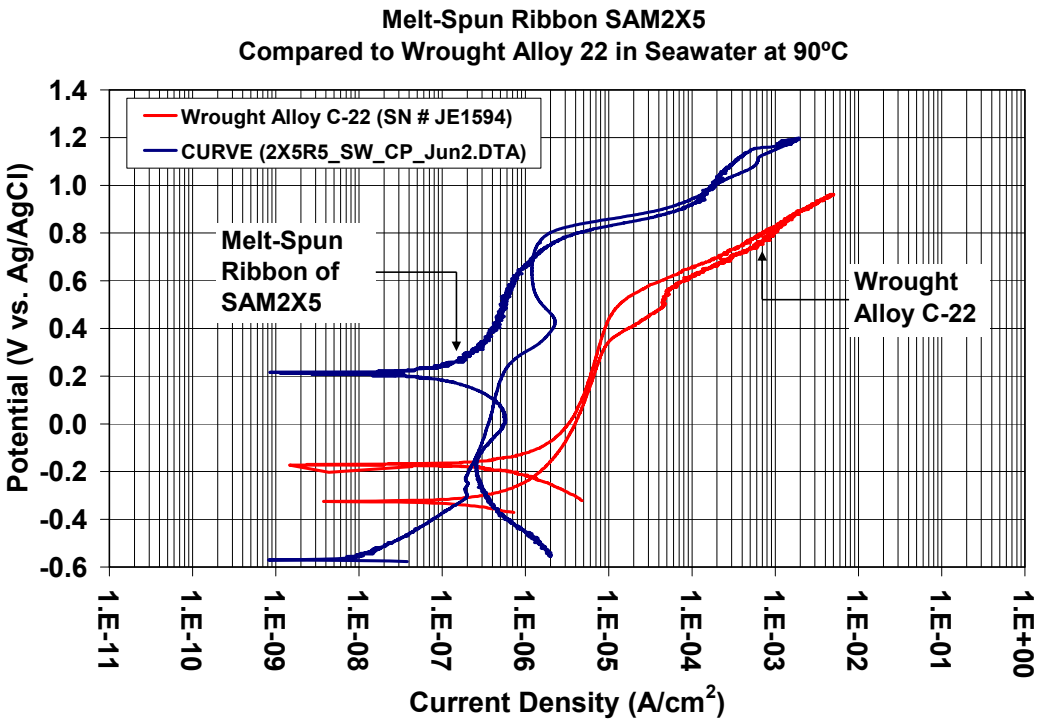

Fig. 7 – This figure shows potential-current data a wrought Alloy C-22 sample and a SAM2X5 MSR in natural seawater at 90°C.

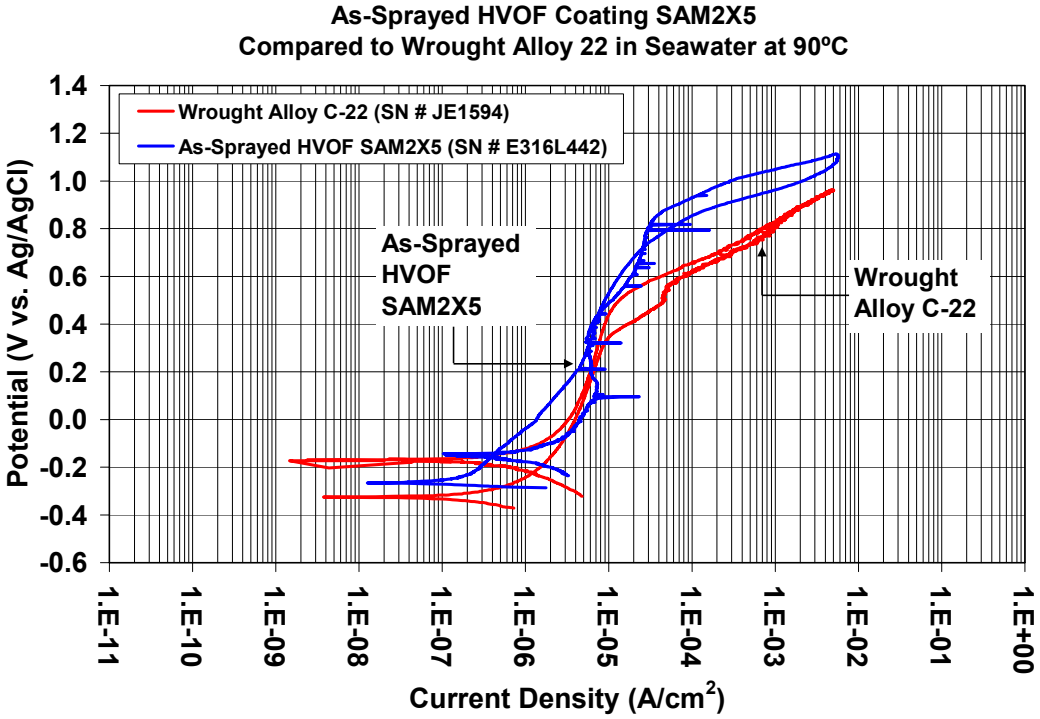

Fig. 8 – This figure shows potential-current data for two wrought Alloy C-22 samples, and an as-sprayed HVOF coating of SAM2X5, which was deposited on a Type 316L stainless steel substrate, in natural seawater at 90°C.

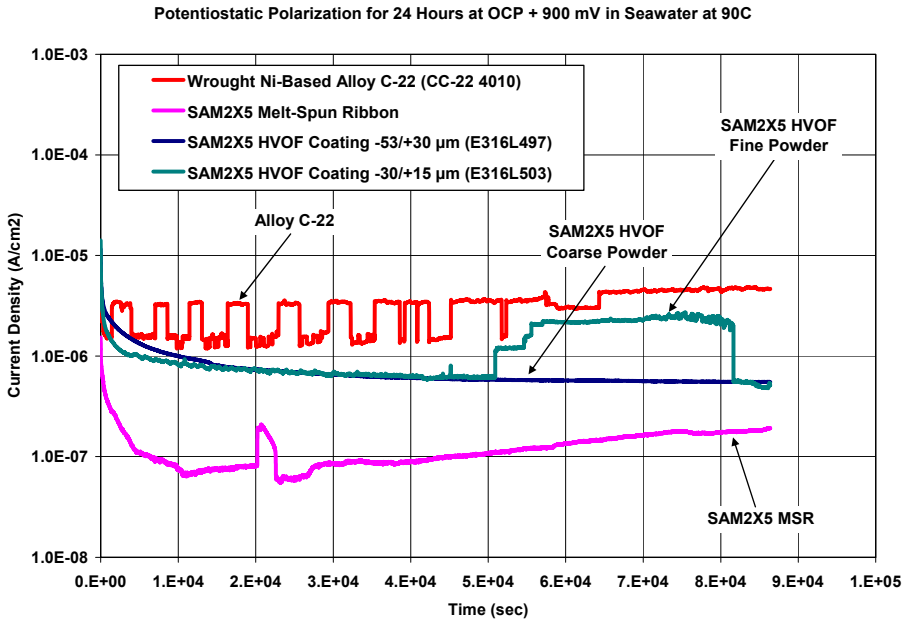

Fig. 9 – Transients in current density at a constant applied potential of 900 mV vs. OCP for wrought Alloy C-22 (reference material), a fully dense and completely amorphous melt spun ribbon (MSR) of SAM2X5, HVOF coatings prepared with –53/+30 micron powders of SAM2X5, and HVOF coatings prepared with –30/+15 micron powders of SAM2X5, all in natural seawater heated to 90°C, are compared.

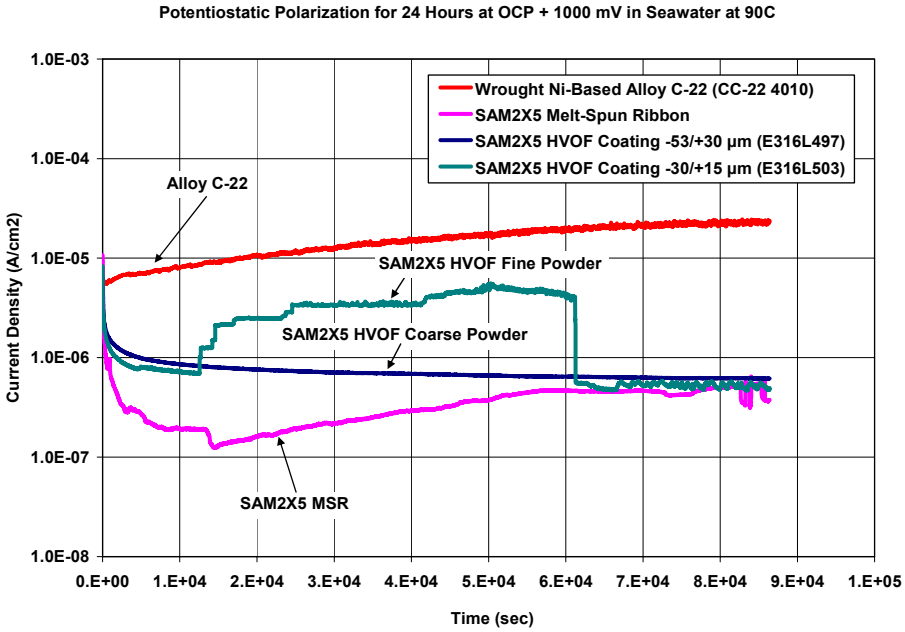

Fig. 10 – Transients in current density at a constant applied potential of 1000 mV vs. OCP for wrought Alloy C-22 (reference material), a fully dense and completely amorphous melt spun ribbon (MSR) of SAM2X5, HVOF coatings prepared with –53/+30 micron powders of SAM2X5, and HVOF coatings prepared with –30/+15 micron powders of SAM2X5, all in natural seawater heated to 90°C, are compared.

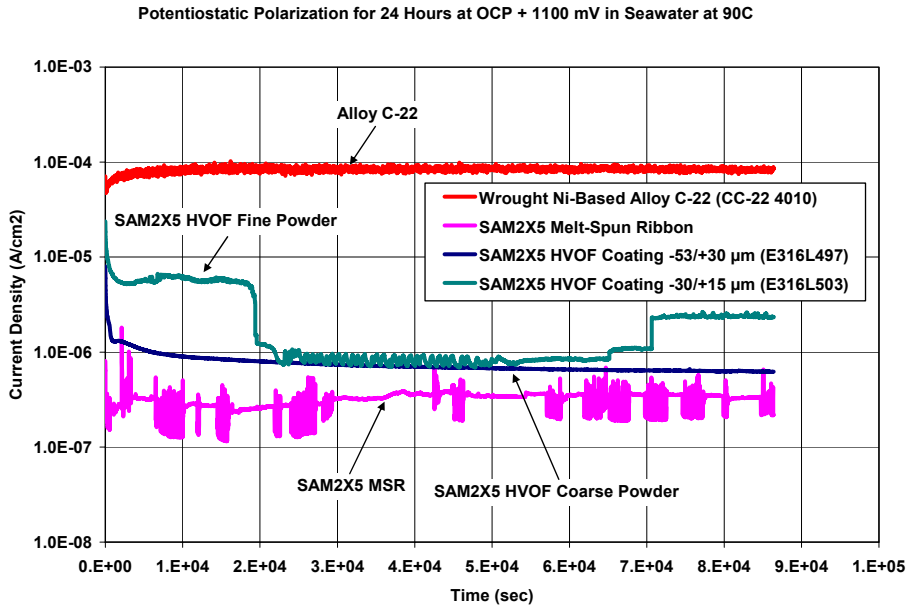

Fig. 11 – Transients in current density at a constant applied potential of 1100 mV vs. OCP for wrought Alloy C-22 (reference material), a fully dense and completely amorphous melt spun ribbon (MSR) of SAM2X5, HVOF coatings prepared with –53/+30 micron powders of SAM2X5, and HVOF coatings prepared with –30/+15 micron powders of SAM2X5, all in natural seawater heated to 90°C, are compared.

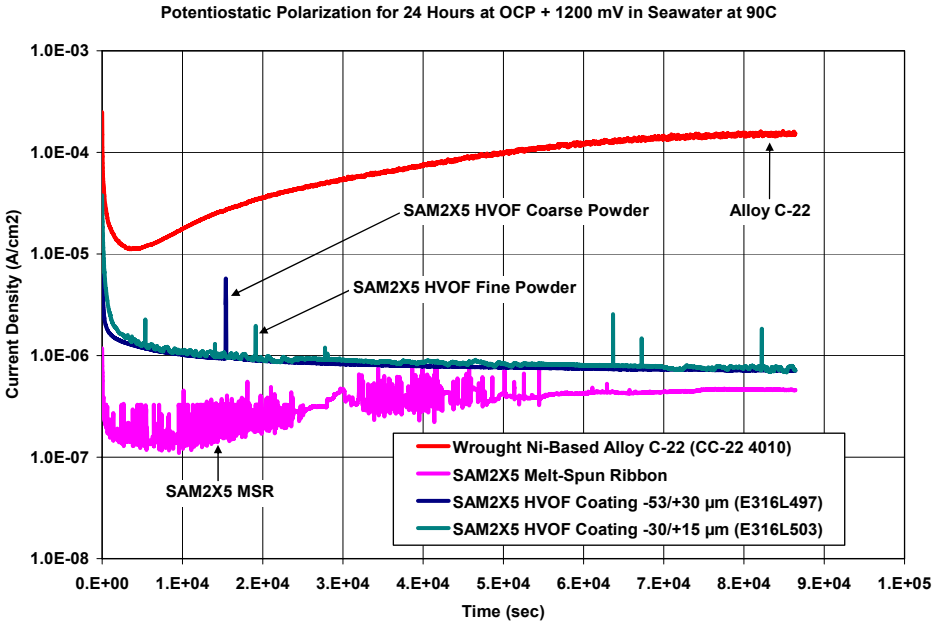

Fig. 12 – Transients in current density at a constant applied potential of 1200 mV vs. OCP for wrought Alloy C-22 (reference material), a fully dense and completely amorphous melt spun ribbon (MSR) of SAM2X5, HVOF coatings prepared with –53/+30 micron powders of SAM2X5, and HVOF coatings prepared with –30/+15 micron powders of SAM2X5, all in natural seawater heated to 90°C, are compared.

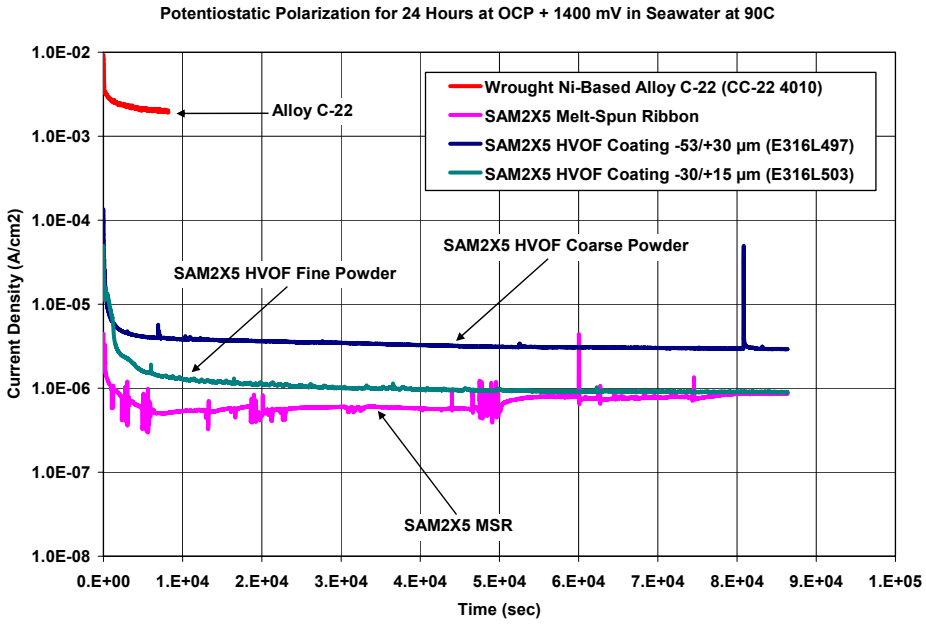

Fig. 13 – Transients in current density at a constant applied potential of 1400 mV vs. OCP for wrought Alloy C-22 (reference material), a fully dense and completely amorphous melt spun ribbon (MSR) of SAM2X5, HVOF coatings prepared with –53/+30 micron powders of SAM2X5, and HVOF coatings prepared with –30/+15 micron powders of SAM2X5, all in natural seawater heated to 90°C, are compared. The Alloy C-22 test was terminated early due to the extent of corrosive attack at the high current density.

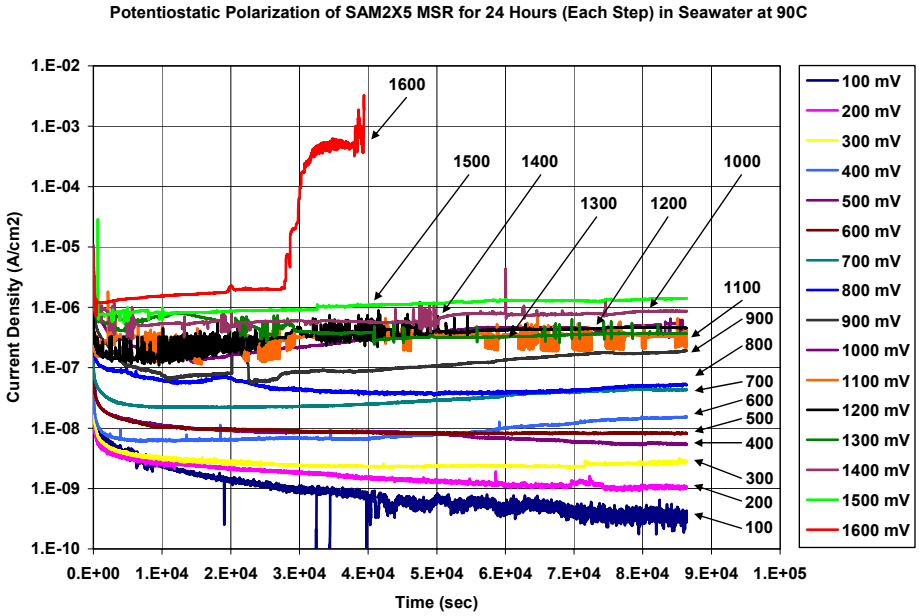

Fig. 14 – Transients in current density at various levels of constant applied potential ranging from 100 to 1600 mV vs. OCP for a melt-spun ribbon of SAM2X5 in natural seawater at 90°C are indicative of good passive film stability.

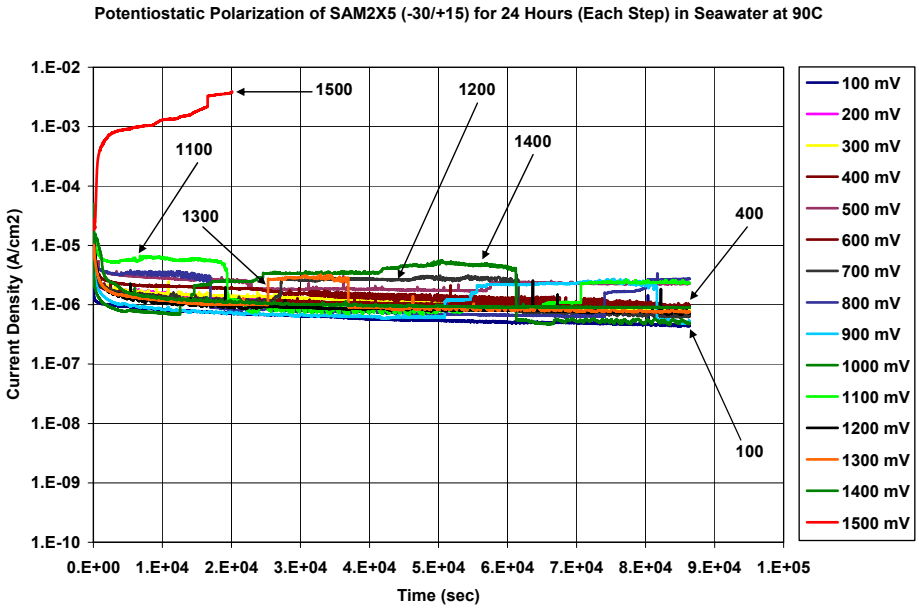

Fig. 15 – Transients in current density at various levels of constant applied potential ranging from 100 to 1500 mV vs. OCP for a recently optimized SAM2X5 HVOF coating (–30/+15 micron powder) in deaerated natural seawater at 90°C are indicative of good passive film stability.

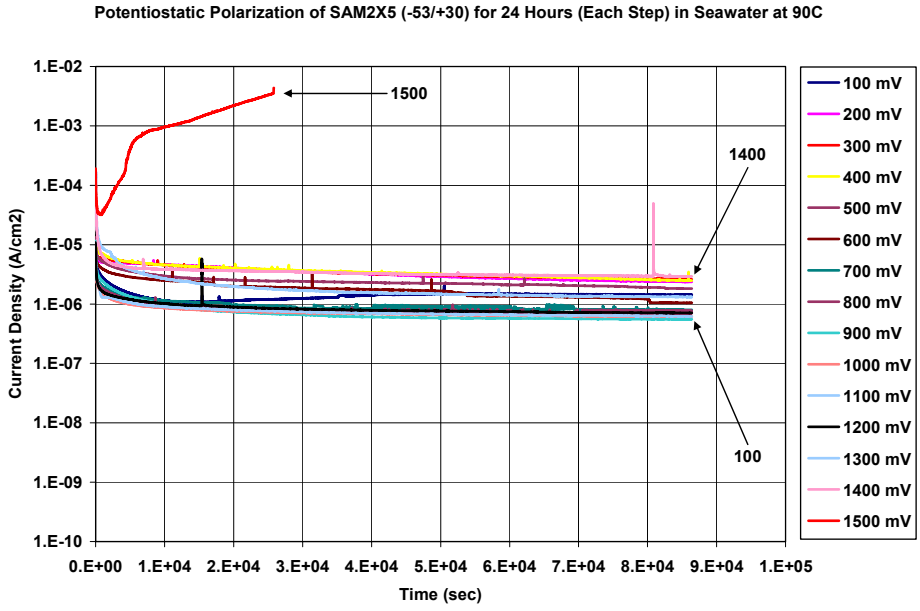

Fig. 16 – Transients in current density at various levels of constant applied potential ranging from 100 to 1500 mV vs. OCP for a recently optimized SAM2X5 HVOF coating (–53/+30 micron powder) in natural seawater at 90°C are indicative of exceptional passive film stability.

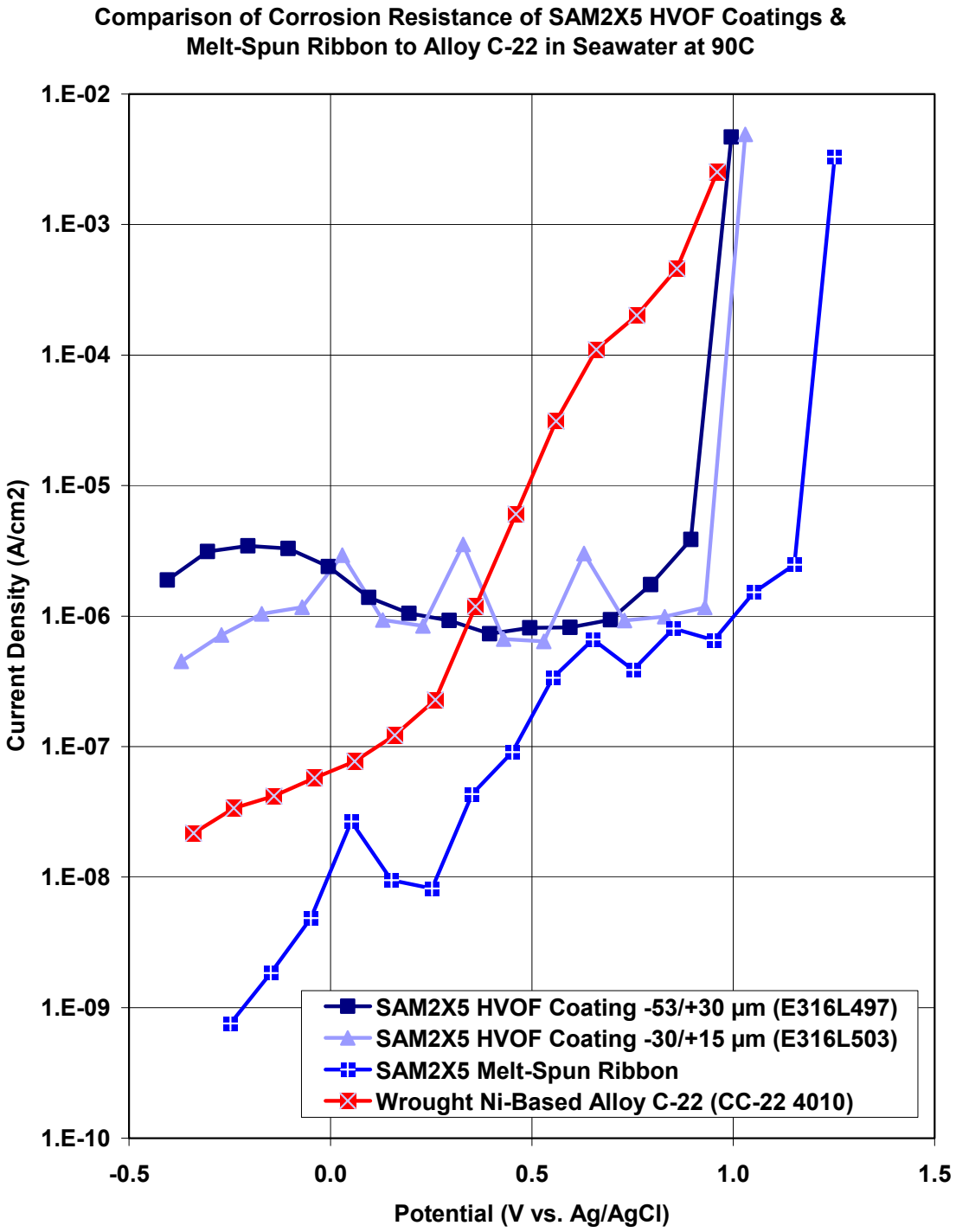

Fig. 17 – Potential-step testing has been performed on wrought Alloy C-22 (reference material); fully dense and completely amorphous melt spun ribbons of SAM2X5; optimized HVOF coatings prepared with –53/+30 micron powders of SAM2X5; and optimized HVOF coatings prepared with –30/+15 micron powders of SAM2X5. All were tested in natural seawater heated to 90°C.

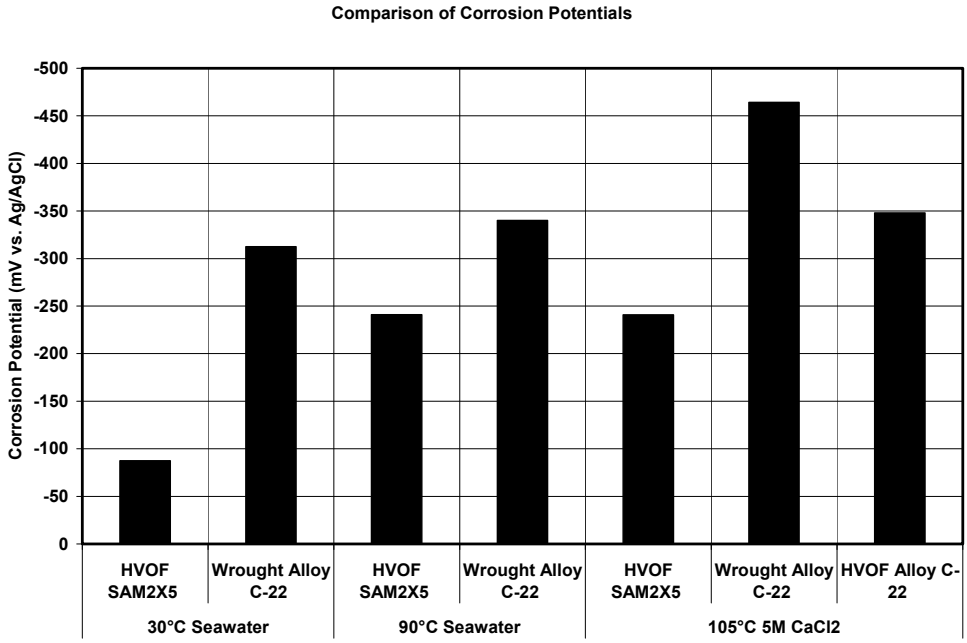

Fig. 18 – The corrosion potentials for the thermal spray coatings of SAM2X5 and the reference material (wrought nickel-based Alloy C-22) in three relevant environments, natural seawater at two temperature levels, and in hot concentrated calcium chloride (5M $CaCl_2$ at 105°C) are summarized.

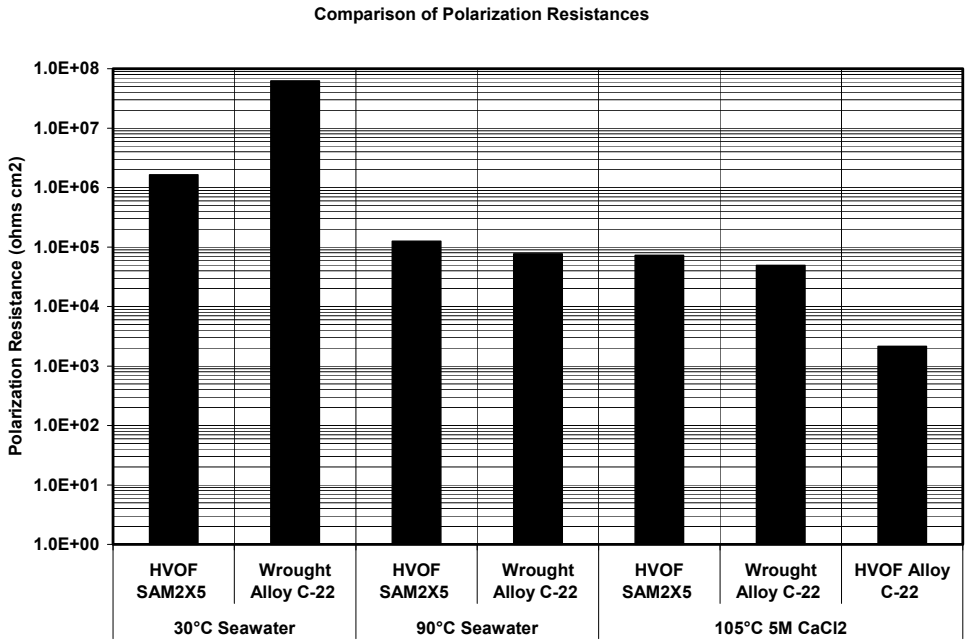

Fig. 19 – Linear polarization was used to determine the polarization resistance for thermal spray coatings of SAM2X5 and the reference material (wrought nickel-based Alloy C-22) in three

relevant environments, natural seawater at two temperature levels, and in hot concentrated calcium chloride (5M $CaCl_2$ at 105°C).

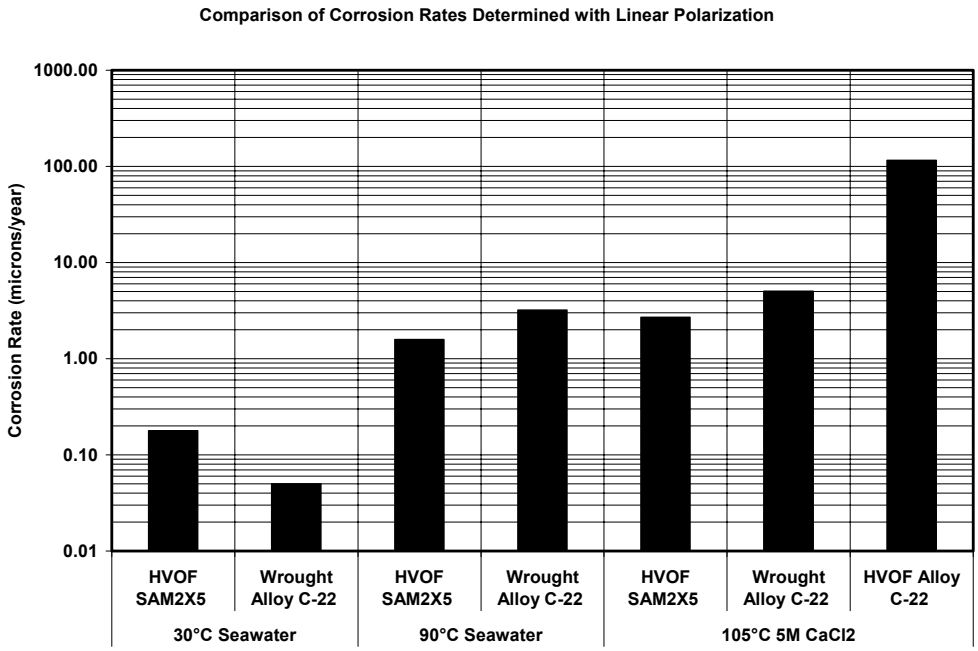

Fig. 20 – Values of the polarization resistance shown in Fig. 25 were converted to corrosion rates for the thermal spray coatings of SAM2X5 and the reference material (wrought nickel-based Alloy C-22) in three relevant environments, natural seawater at two temperature levels, and in hot concentrated calcium chloride (5M $CaCl_2$ at 105°C).

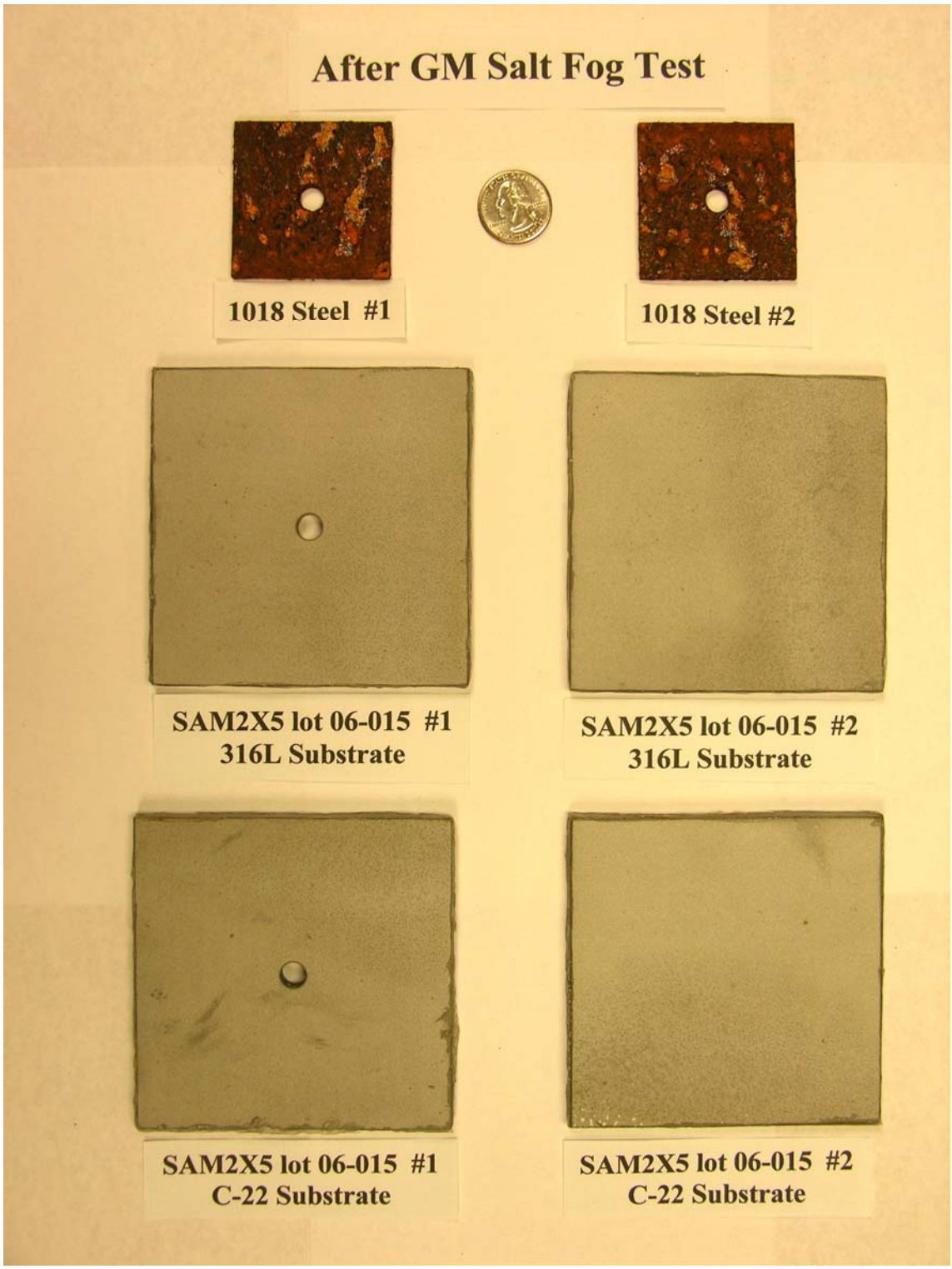

Fig. 21 – Results of salt-fog testing of SAM2X5 thermal-spray coatings and 1018 carbon steel control samples. No corrosion of the SAM2X5 coatings was observed after eight cycles, while the 1018 carbon steel samples experienced severe attack.